minerals

MDPI

Article

The Arkansas Alkaline Province, Southeastern USA: A Synthesis of New and Existing Chemical and Petrologic Data and Petrogenetic Considerations

Nelson Eby [1,*], Norman Charnley [2,†], Gino Tiella [1] and Louis Burkhardt [1]

[1] Department of Environmental, Earth and Atmospheric Sciences, University of Massachusetts, Lowell, MA 01854, USA; gtiella@londonderry.org (G.T.); chipburkhardt@yahoo.com (L.B.)
[2] Department of Earth Sciences, University of Oxford, Oxford OX1 3AN, UK; norman.charnley@retired.ox.ac.uk
* Correspondence: nelson_eby@uml.edu
† This author was retired.

Abstract

The Arkansas alkaline province (AAP), southeastern US, consists of seven intrusions or intrusive complexes that lie along a NE–SW trend that falls on the extension of the Mississippi Valley graben. There are three distinct magmatic events: (1) emplacement of lamproites at ~104 Ma, (2) emplacement of lamprophyres, phonolites, carbonatites, ijolites, and a variety of nepheline syenites between 100 and 98 Ma, and (3) emplacement of a large nepheline syenite body at ~88 Ma. Unpublished and published mineralogical, elemental, and isotope data are used to develop an integrated model for the AAP magmatic activity. The lamproites were derived from ancient enriched subcontinental lithosphere. The carbonatite–lamprophyre–phonolite–ijolite–nepheline syenite association comprises several intrusive complexes (Magnet Cove, Potash Sulphur Springs, V-intrusive) and the Benton lamprophyre–felsic dike swarm. Magmatic evolution is controlled by fractional crystallization of pyroxene and nepheline. The carbonatites may be the result of liquid immiscibility between carbonate and lamprophyric liquids. The large nepheline syenite body (Granite Mountain and Saline County) evolved through fractional crystallization of feldspar and nepheline. Event 2 and 3 magmas were derived from an OIB-like asthenospheric source. The most likely model for the origin of the AAP is the reactivation of a zone of crustal weakness by far field stresses.

Keywords: Arkansas Alkaline Province; carbonatite; lamprophyre; nepheline syenite; mineral chemistry; rock chemistry; radiogenic isotopes; petrogenesis

Academic Editor: Dmitry Konopelko

Received: 24 September 2025
Revised: 23 October 2025
Accepted: 25 October 2025
Published: 29 October 2025

Citation: Eby, N.; Charnley, N.; Tiella, G.; Burkhardt, L. The Arkansas Alkaline Province, Southeastern USA: A Synthesis of New and Existing Chemical and Petrologic Data and Petrogenetic Considerations. *Minerals* **2025**, *15*, 1133. https://doi.org/10.3390/min15111133

1. Introduction

Cretaceous age alkaline rocks are widespread throughout the northern Gulf of Mexico basin, southeastern United States. These occurrences are largely subsurface and are encountered in drill holes in southeast Oklahoma, south-central Texas, northeast Louisiana, southeast Arkansas, and west-central Mississippi [1]. The four major groups of subsurface volcanic and hypabyssal rocks are trachytes, phonolites, alkaline basalts, and lamprophyres [2]. Ar-Ar ages for these rocks range from 67.2 to 80.7 Ma [3]. The major surface exposures of alkaline rocks occur in the Arkansas alkaline province (AAP) which consists of seven intrusions or intrusive complexes that lie along a NE–SW trend that falls on the extension of the Mississippi Valley graben (Figure 1). The lithologies found in these intrusions are lamproite, carbonatite, jacupirangite, ijolite, a variety of nepheline syenites,

phonolites, and lamprophyre dikes. Volumetrically, Granite Mountain and Saline County nepheline syenite bodies are the major intrusive complexes in the AAP. Radiometric ages for the AAP range from 108 Ma to 88 Ma (Table S1). Volcanoclastic sediments in southwest Arkansas (the Woodbine Volcanoclastics) primarily contain phonolite and trachyte cobbles with lesser trachybasalt cobbles. Ar-Ar ages of 93.9 to 95.3 Ma [3] for these clasts indicate that they represent eroded AAP lithologies. A number of petrogenetic models have been proposed for the origin of the AAP: (1) passage of the continental plate over a hotspot [4–6], (2) activation of zones of lithospheric weakness due to far field stress [7], (3) sheet-like mantle upwellings induced along slab window margins [8], and (4) edge-driven convection [9].

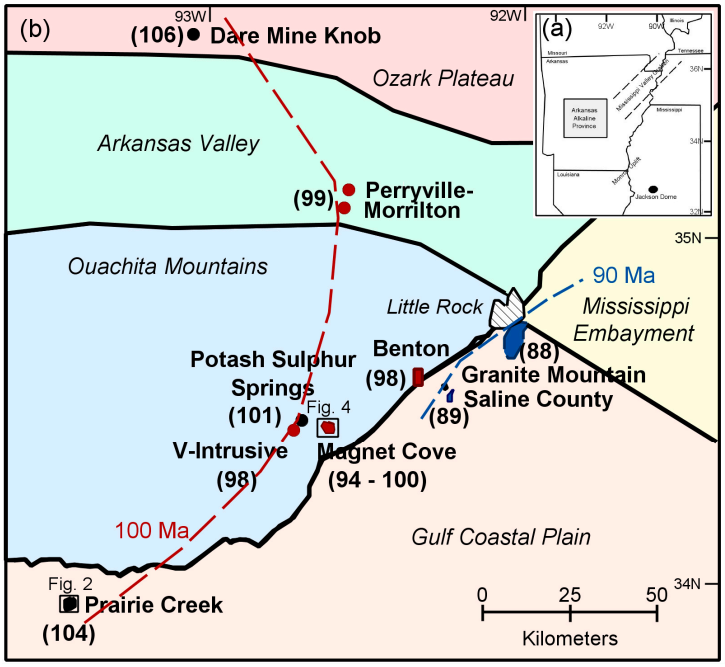

Figure 1. Map of Arkansas Alkaline Province modified from [7]. (**a**) Inset showing position of AAP in the southeastern US. (**b**) Location of the intrusions. Number in parenthesis is the best age estimate (in Ma) for the intrusion. Radiometric ages for Magnet Cove, using fission-track, Ar-Ar, and U-Pb mineral dating, vary from 94 to 100 Ma. The dashed red and blue lines denote geochronological boundaries. Intrusion color denotes age group—black, older than 100 Ma; red, 100–94 Ma; and blue, 90–87 Ma.

In this paper we report new mineralogical and rock chemical data for the AAP. These data are combined with results from other studies in an effort to present a unified petrogenetic model for the province.

2. Geology and Petrography

The various intrusions of the Arkansas province were emplaced into the folded and faulted lower to middle Paleozoic rocks of the Ouachita Mountain fold belt. The fold belt is cored by the Benton uplift (Upper Cambrian to Lower Mississippian rocks) which is enclosed by Upper Mississippian and Lower Pennsylvanian rocks, all of which have been strongly folded [10]. The rocks of the Benton uplift are predominantly shales, clastic and carbonate sandstones, cherts, and conglomerates (e.g., Ordovician Womble Shale, Devonian Arkansas Novaculite, and Mississippian Stanley Shale). An erosional surface of Middle Cretaceous age separates these rocks from the overlying Upper Cretaceous to Holocene sediments of the Mississippian embayment.

2.1. Dare Mine Knob

Dare Mine Knob is located approximately 120 km northwest of Little Rock, Arkansas (Figure 1) and comprises lamproite. Lamproites are K-rich volcanic to subvolcanic rocks, often porphyritic with olivine, phlogopite, and/or leucite phenocrysts, in a fine-grained or glassy groundmass. The Dare Mine Knob lamproite is fine-grained and the primary minerals are pyroxene (altered to serpentine) and amphibole. The matrix largely consists of chlorite. Minute perovskite crystals are abundant.

2.2. Prairie Creek Lamproite Province

Diamond-bearing olivine lamproites occur in Pike County, Arkansas. Seven diamondiferous vents extend for 5 km in a northeasterly direction from the largest vent, the Prairie Creek complex. Twin Knobs #1 lamproite is approximately 300 m NE of Prairie Creek and consists of lamproite, sandy tuffs and breccias, and epiclastics [11]. Twin Knobs #2 is approximately 500 m NE of Prairie Creek and Black Lick is approximately 1000 m NE of Prairie Creek. The rock types for both are the same as Twin Knobs #1. Xenoliths of mantle and crustal rock were recovered from the Twin Knobs #2 and Black Lick lamproites. The mantle xenoliths include dunite, harzburgite, websterite, wehrlite, eclogite, spinel lherzolite, and garnet lherzolite [12]. About half the crustal xenoliths are near surface crustal lithologies and the crystalline crustal xenoliths are ~50% amphibolites, ~5% pelitic metamorphic rocks, ~5% are granitic/rhyolitic, and the remaining ~40% are epidote-rich varieties [13].

The Prairie Creek complex (Figure 2) consists of four units: olivine lamproite which comprises slightly more than 50% of the exposure, phlogopite-rich and olivine-rich lamproite tuff (~40% of the exposure), and epiclastic rocks (a minor component) [12,14]. A lamproite dike intrudes the tuff and, thus, the tuff is the oldest unit in the complex. Diamond mining has occurred sporadically and the largest diamond discovered weighed 15.33 carats [15]. Diamonds are frequently found in the tuff.

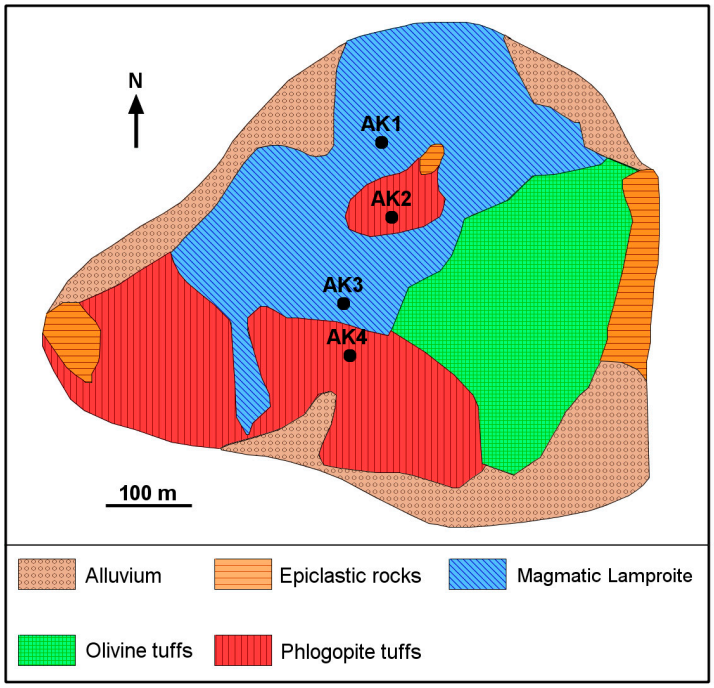

Figure 2. Geological map of the Prairie Creek complex modified from [12]. Bold labels show locations of sample sites.

The lamproite (Figure 3) consists of olivine and lesser diopside macrocrysts (both are corroded and the olivines have serpentine reaction rims) in a glassy groundmass now substantially altered to serpentine, chlorite, poikilitic phlogopite, and dispersed small crystals of diopside, apatite, Cr-spinel, and perovskite. Rare phases are potassic richterite, priderite, high-Cr garnet, and low-Cr garnet [16].

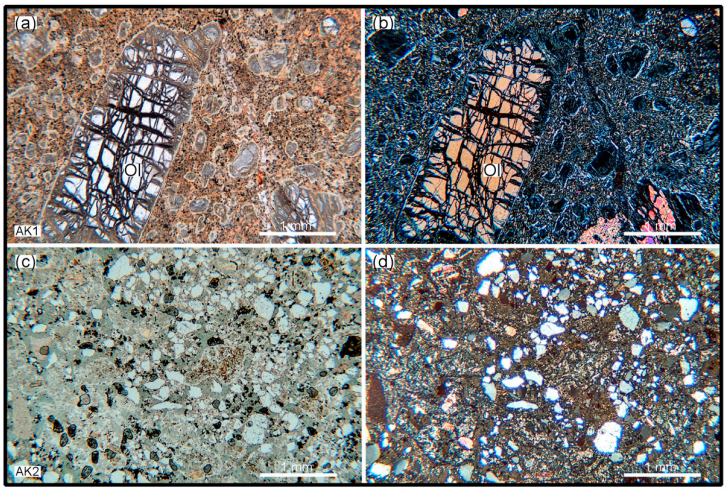

Figure 3. Prairie Creek lamproite and tuff thin section images. Lamproite (AK1) in (**a**) plane light and (**b**) crossed polars. Olivine phenocrysts in a serpentine and chlorite glassy groundmass. Tuff (AK2) in (**c**) plane light and (**d**) crossed polars. Crustal xenoliths in a serpentine and chlorite matrix. Mineral abbreviations here and in other images from [17].

The tuff units (Figure 3) are significantly altered and deeply weathered. They consist of a highly variable combination of juvenile lapilli, ultramafic autoliths, crustal xenoliths, and olivine macrocrysts in a serpentine and chlorite matrix.

The epiclastic rocks are blue in color and contain rock fragments and lapilli in a chlorite-rich matrix. Quartz grains occur locally and are apparently derived from the underlying Jackford sandstone. Graded bedding in some units suggests a water laid origin.

2.3. Magnet Cove

The Magnet Cove complex (Figure 4) consists of a core of ijolite and calcite-carbonatite, which is surrounded, in turn, by a U-shaped body of phonolite and an outer ring of syenite [18]. Jacupirangite is found in two localities in the outer ring. The proposed sequence of intrusion [18] is (1) phonolite, (2) jacupirangite, (3) outer-ring syenites, (4) ijolite, and (5) calcite-carbonatite. Subsequent work [19,20] indicates that there are several generations of syenite and that the sequence of intrusion proposed by Erickson and Blade [18] requires modification. Using ground-based gravity and magnetic data, two-dimensional and three-dimensional geophysical models have been developed for the Magnet Cove complex [21]. These models show the Magnet Cove complex widening out at middle crustal depths to a width of 22 km and the intrusion may reach a depth of 20 km.

The calcite-carbonatite is coarse-grained and consists of calcite, green phlogopite, monticellite, rare pyroxene or amphibole, and the accessory minerals high-Nb perovskite, magnetite, apatite, and Zr-garnet. The ijolite (Figure 5) is medium- to coarse-grained and consists of varying amounts of diopside, biotite, nepheline, and garnet and as accessory minerals titanite and apatite. Depending on the relative proportions of pyroxene, the lithology varies from ijolite to melteigite. The phonolite is fine-grained and consists of orthoclase or sanidine, nepheline, sodalite, hornblende, diopside, titanite, apatite, and minor andesine. Flohr and Ross [22] also identified outcrops of nepheline syenite within the phonolite unit and these rocks were chemically and/or mineralogically distinct from

other syenites in the complex. The outer-ring syenite (Figure 5) is predominantly nepheline syenite with lesser garnet pseudoleucite syenite. The syenites contain orthoclase, nepheline, zoned pyroxene, hornblende, alkali amphiboles, apatite, magnetite, and variable amounts of titanite and melanite. Sodalite is found as a late-magmatic to deuteric mineral. Flohr and Ross [19] subdivided the outer ring syenite into six types: (1) Diamond Jo nepheline syenite, (2) pseudoleucite-nepheline syenite, (3) garnet-nepheline syenite, (4) titanite (sphene)-nepheline syenite, (5) alkali syenite, and (6) miscellaneous nepheline syenites. The jacupirangite is coarse-grained and consists of magnetite with perovskite rims and zoned pyroxene. A lamprophyre dike occurs adjacent to the complex. The lamprophyre consists of amphibole and pyroxene phenocrysts in a fine-grained groundmass of the same minerals plus feldspar (Figure 5).

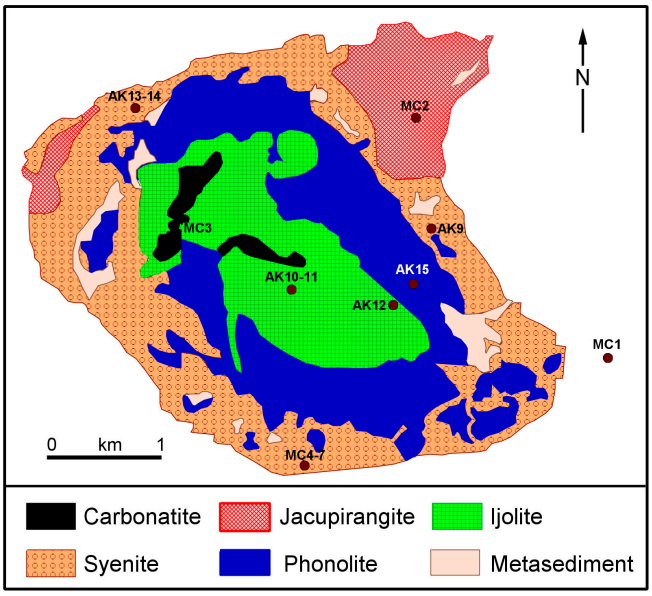

Figure 4. Geological map of the Magnet Cove complex. Modified from [7]. Bold labels show locations of sample sites.

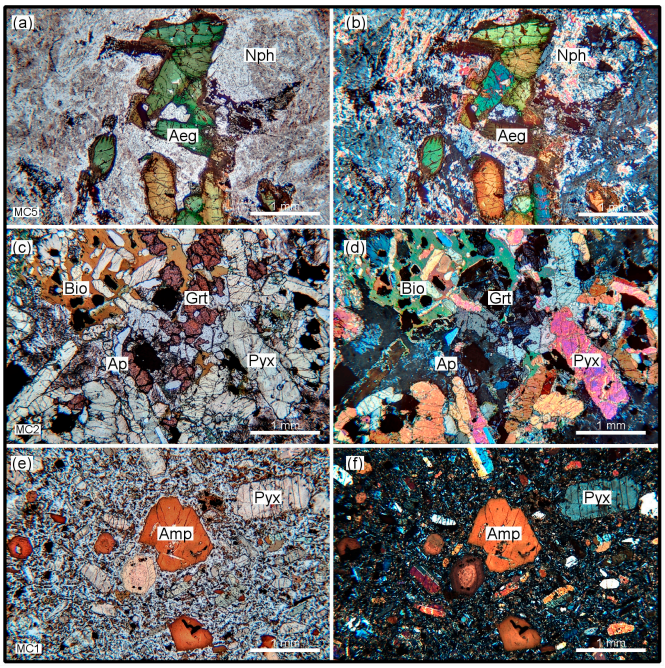

Figure 5. Magnet Cove nepheline syenite, ijolite, and lamprophyre thin section images. Nepheline syenite (MC5) in (**a**) plane light and (**b**) crossed polars. Aegerine, nepheline, and feldspar. There is

substantial alteration of nepheline to cancrinitel (high birefringence material). Ijolite (MC2) in (**c**) plane light and (**d**) crossed polars. Diopside, biotite, nepheline, and garnet with accessory apatite. Lamprophyre (MC1) in (**e**) plane light and (**f**) crossed polars. Amphibole and pyroxene phenocrysts in a fine-grained groundmass of the same minerals plus feldspar. Mineral abbreviations from [17].

2.4. Potash Sulphur Springs

The complex is located 8 km west of Magnet Cove, has a small areal extent (0.65 km^2), and largely consists of feldspathoidal syenite with lesser nepheline alkali-feldspar syenite (pulaskite), ijolite, calcite-carbonatite, and late-stage lamprophyre and syenite dikes [20,23]. Fenitization of the surrounding silica-rich novaculite was pervasive and this was thought to be caused by fluids escaping from the calcite-carbonatite [24]. This fenitization was responsible for the development of vanadium ore deposits in the novaculite.

The feldspathoidal syenite is largely composed of alkali feldspar and nepheline with minor amounts of biotite, aegirine, aegirine-augite, melanite, titanite, apatite, and sodalite. The ijolite consists of nepheline and augite, which is replaced and mantled by aegirine, and minor alkali feldspar, sodalite, calcite, titanite, and ilmenite. On a mineralogical basis [25] four calcite-carbonatite units were identified: phlogopite sovite, alvikite, ferriphlogopite sovite, and sovite pegmatite, arranged in order of intrusion from oldest to youngest. Clinopyroxene is also found in the carbonatite and its occurrence is attributed to the mixing of ijolite and carbonatite magmas [26].

2.5. V-Intrusive

The V-intrusive lies 10 km southwest of Magnet Cove, occupies an area of approximately 0.5 km^2, and consists of at least 40 cross-cutting dikes that show a V-shaped pattern on a geologic map [27]. The suggested sequence of emplacement, from oldest to youngest, is malignite, melteigite, microijolite, tinguaite porphyry, sannaite, melanite nepheline syenite, pyroxene nepheline syenite, nepheline syenite, phonolite, and aplite veins of fluorite, pyrite, and silica [27]. Individual rock names are determined by the relative amounts of mafic and felsic minerals, which include olivine, clinopyroxene with complex zoning, alkali feldspar, and nepheline. Accessory minerals are biotite, titanite, perovskite, rutile, zircon, magnetite, ilmenite, fluorite, apatite, and calcite.

2.6. Benton Dike Swarm

Lamprophyre and felsic dikes are abundant within a 350 km^2 area north of Benton, Arkansas. The dikes are 1 to 2 m wide, 100 m to 2 km in mapped length, and generally trend east–west. The lamprophyre dikes (using the original study nomenclature) are predominantly monchiquite, melamonchiquite, and ouachitite, with lesser camptonite and sannaite [28,29] (Figure 6). *Monchiquites* contain olivine, pyroxene, and usually biotite and/or amphibole phenocrysts in a groundmass of glass or analcime. *Melamonchiquite* is similar to monchiquite but with more abundant mafic minerals. *Ouachitite* (a local name) has phlogopite phenocrysts (±olivine, clinopyroxene, amphibole) in a matrix of similar minerals. *Camptonite* has pyroxene and amphibole phenocrysts in a groundmass of the same minerals plus plagioclase. *Sannaite* has amphibole, pyroxene, and biotite phenocrysts in a fine-grained groundmass of alkali feldspar, chlorite, and nepheline. The felsic dikes are variably weathered and have been classified as microsyenites. Lamprophyre and felsic (microsyenite and phonolite) dikes and carbonatites were encountered in drill holes in the Benton area [30].

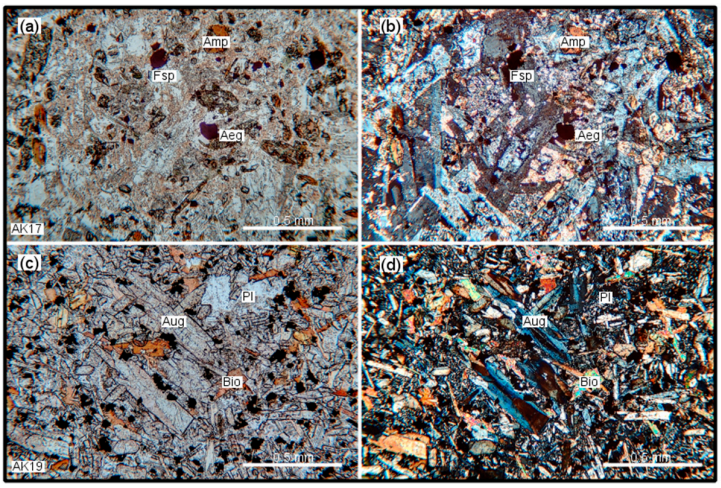

Figure 6. Benton felsic dike and lamprophyre (ouachitite) thin section images. Felsic dike (AK17) in (**a**) plane light and (**b**) crossed polars. The major minerals are aegirine, amphibole, and feldspar. Lamprophyre (AK19) in (**c**) plane light and (**d**) crossed polars. Large pyroxene and biotite grains in a finer grained matrix of amphibole, biotite, and feldspar. Mineral abbreviations from [17].

2.7. Saline County and Granite Mountain Syenites

Major surface exposures of syenite occur near the town of Bauxite in Saline County and just south of Little Rock at Granite Mountain. Drill core and geophysical data [31] suggest that the syenite body may be continuous at depth with an areal extent of 300 km^2.

A study by Bath [32] of an abandoned quarry in Saline County revealed two syenite lithologies: a nepheline-sodalite syenite and a nepheline alkali-feldspar syenite. The nepheline-sodalite syenite was volatile-rich and crystallized at shallow depth from the roof downward. The surrounding country rock was locally fenitized, presumably due to fluids from the nepheline-sodalite syenite. The nepheline alkali-feldspar syenite represents a later intrusive phase and the nepheline-sodalite syenite occurs in the nepheline alkali-feldspar syenite as a stoped roof block (Figure 7).

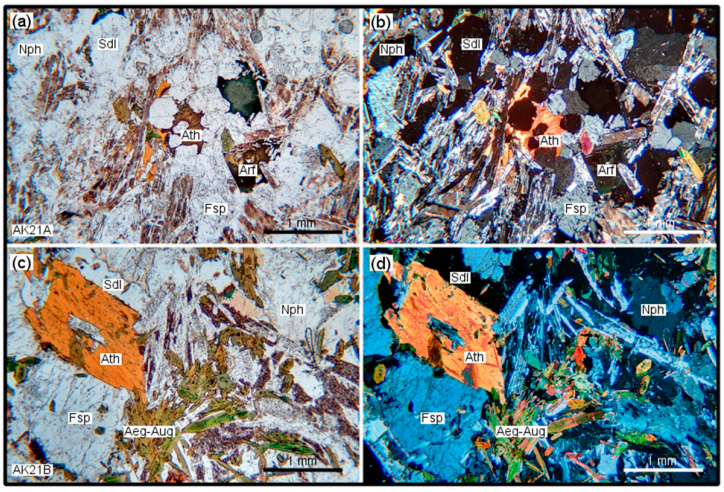

Figure 7. Saline County nepheline syenite and pegmatitic nepheline thin section images. Nepheline syenite (AK21A) in (**a**) plane light and (**b**) crossed polars. Medium-grained. Major mineralogy is arfvedsonite, anthophyllite, nepheline, sodalite, and feldspar. Coarse-grained (pegmatitic) nepheline syenite (AK21B) in (**c**) plane light and (**d**) crossed polars. Large anthophyllite grains. Radiating elongate grains of aegirine-augite and feldspar. Interstitial sodalite. Mineral abbreviations from [17].

The Granite Mountain complex is located just south of Little Rock, AR, has an areal exposure of ~12 km^2, and consists of medium- to coarse-grained syenites that can be

subdivided into five principal lithologies: olivine syenite, dark gray syenite, light gray syenite, syenite pegmatite, and rare quartz syenite [33]. The bulk of the complex consists of the dark and light gray syenites, which are intimately mixed and co-mingled. Contacts with the country rock are sharp and a 10 m wide chilled margin shows flow-aligned alkali feldspar phenocrysts. The olivine syenite occurs as irregularly distributed "blobs" with diameters less than 1 m. The olivine syenite contains 1 to 2% olivine (Fo70), 10–15% euhedral diopside, 2–5% biotite, trace ilmenite, and >80% alkali feldspar (some with plagioclase, An30, cores).The dark gray syenite contains no olivine, ilmenite, or relict plagioclase and mineralogically consists of alkali feldspar (anorthoclase to orthoclase), diopside, biotite, nepheline, titanite, and magnetite. The light gray syenite occurs as veins and blobs within the dark gray syenite and mineralogically consists of alkali feldspar (microperthite and orthoclase), biotite, diopside, amphibole, titanite, magnetite, nepheline, and analcime. The pegmatite has a pink hue and forms discrete, sharply bounded veins and dikes up to 20 m wide and 1000 m long. Mineralogically the pegmatite consists of sodic anorthoclase, acmite, zeolites, fluorite, and a variety of rare minerals (Figure 8). More than 75 minerals have been identified in the Granite Mountain complex [34].

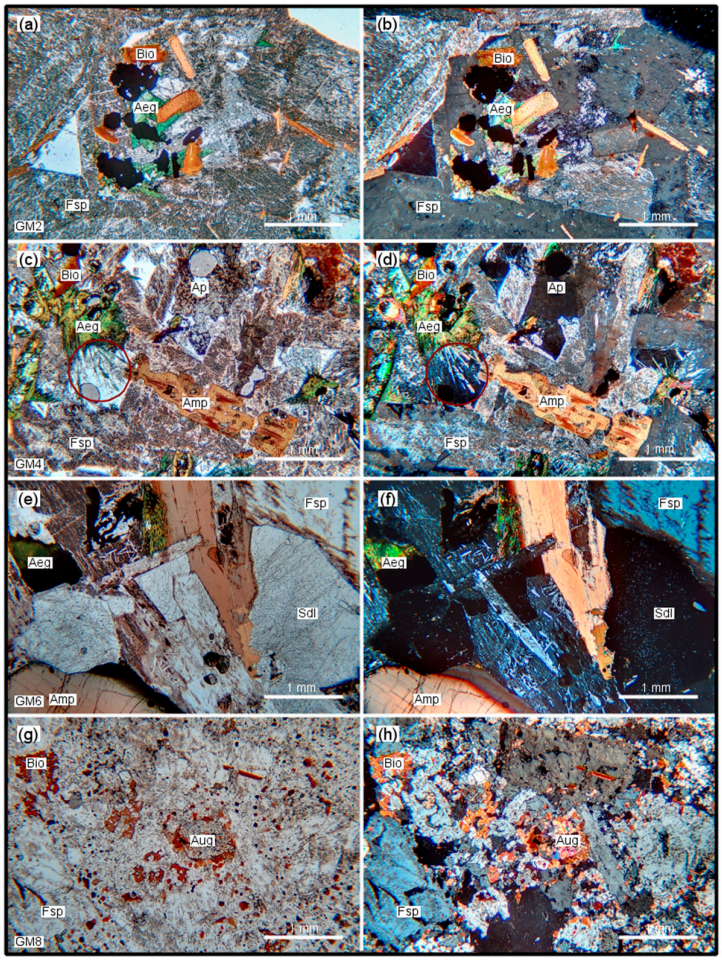

Figure 8. Granite Mountain syenite thin section images. Medium-grained syenite (GM2) in (**a**) plane light and (**b**) crossed polars. Aegirine, biotite, feldspar, and opaque minerals. Medium-grained pink syenite (GM4) in (**c**) plane light and (**d**) crossed polars. Biotite, aegirine, amphibole, feldspar, and accessory apatite. Area inside red circle shows elongate aegirine laths which apparently grew into a fluid-filled cavity. Pegmatitic syenite (GM6) in (**e**) plane light and (**f**) crossed polars. Large amphibole, feldspar, and sodalite grains. Interstitial aegirine. Medium-grained syenite (GM8) in (**g**) plane light and (**h**) crossed polars. Biotite, augite, and perthitic feldspar. Minor olivine (not seen in this image). Mineral abbreviations from [17].

2.8. Morrilton and Perryville Carbonatite Dikes

Thin calcite-carbonatite dikes (<1 m in width) crop out 70 to 80 km north of Magnet Cove. The dikes are xenocrystic alvikite breccias. The xenocrysts are granite, syenite, magnetite-apatite rock, sovite, and phlogopite. The groundmass consists of a finely crystalline mosaic of calcite and apatite with moderate amounts of magnetite, phlogopite, and dolomite and accessory amounts of perovskite, zircon, and pyrite [35].

3. Geochronology

Radiometric ages for the AAP intrusions were determined using a variety of dating systems—fission-track, K-Ar, Ar-Ar, Rb-Sr, and U-Pb. The results from the different methods are listed in Table S1. The mean ages are shown on the AAP location map (Figure 1).

Three K-Ar phlogopite ages for the Prairie Creek lamproite fall between 99 and 108 Ma [36,37]. The weighted mean age for the three determinations is 104 ± 5 Ma. Within error, this age agrees with the 106 Ma for the Dare Mine Knob lamproite [7].

A number of ages are reported for Magnet Cove (Table S1) and the ages range from 90 to 105 Ma [3,7,36,38–41]. Argon–argon mica ages, presumably the most precise, are 94.4 ± 0.2 Ma (biotite/ijolite), 94.2 ± 0.2 Ma (biotite/jacupirangite), and 94.3 ± 1.0 (phlogopite/carbonatite) [7,39]. A recent U-Pb study [40] yields the following preliminary ages: perovskite/carbonatite 100.5 ± 1.7 Ma, garnet/syenite 101.4 ± 0.8 Ma, and garnet/ijolite 98.1 ± 0.6, 102.8 ± 0.6 Ma. For each dating method the ages are statistically identical, implying that the Magnet Cove magmas were emplaced in a very short time span, but the ages are offset by 6 million years (94.3 Ma Ar-Ar and 100.5 Ma U-Pb). For Perryville–Morrilton [7], Potash Sulfur Springs [7,42], the V-intrusive [7], and the Benton dike swarm [7] ages range between 97 Ma and 101 Ma (Table S1), similar to the older U-Pb ages determined for Magnet Cove.

Ages determined for the syenite bodies in Saline County [7] and at Granite Mountain [3,7,36,39] range between 88 and 94 Ma (Table S1). The mean age for Saline County is 89 ± 2 Ma and for Granite Mountain the mean age is 89.5 ± 2 Ma.

Based on the radiometric data, three age groups are identified. The lamproites are emplaced at ~104 Ma, the carbonatites and associated silicate rocks at ~100 Ma (the older U-Pb ages are used for Magnet Cove), and the nepheline syenite bodies at ~88 Ma.

4. Materials and Methods

Samples collected for this study varied in size from 0.5 to several kilograms. In the Supplemental Data Tables S2 and S3 these samples are identified with the prefixes AK, DMK, GM, KL, MC, and Mu. Isotopic data for the samples is already published [8]. In this study, mineral chemistry and major and trace element whole-rock chemistry is reported. Other data reported in the Supplemental Tables are from the published literature [8,19,22,33,43–46], theses [28], and United States Geological Survey Open File Reports. The U. S. Geological Survey investigated three areas: Magnet Cove, Potash Sulfur Springs, and Benton, Arkansas. The Magnet Cove samples [47] are from drill core M5 (Molycorp, Inc., Mountain Pass, CA, USA) located in the northwest corner of Section 19, TS3, R17W. The total depth of the drill core was 750 feet (228.6 m). The Potash Sulfur Springs samples [26] are from drill core M162 (Union Carbide Corporation) and surface outcrops. The total depth of the drill core was 560 feet (170.7 m). The complex is located in Garland County, Arkansas (W½, Section 17 and E½, Section 18, TS3, R18W). The Benton, Arkansas samples [30] are from seven drill cores. Location details are given in the open file report [30].

Slabs were cut from each sample for thin sections and polished probe sections. Mineral chemistry was determined using a Cambridge Scientific Instruments Microscan 9 electron

microprobe, Cambridge, UK. A variety of pure metals, oxides, and well-characterized natural silicates were used as standards. Analyses were conducted at 20 kV accelerating potential, 35 nA beam current, and a spot size of 5–10 μm. The measurements were corrected for atomic number, absorption, and fluorescence (ZAF correction).

Powders for chemical analysis were prepared by crushing rock chips in a jaw crusher with hardened steel plates, followed by reduction to finer size using a pulverizer with ceramic plates, and then hand grinding to a fine powder in a ceramic mortar and pestle.

Major element rock chemistry was obtained by standard X-ray fluorescence (XRF) techniques, using fusion beads, at the University of Queensland, Australia. Loss on ignition was determined by heating one gram of material to 1000 °C for one hour. Fe^{2+} was determined by titration [48].

The concentrations of V, Cr, Ni, Cu, Zn, Rb, Sr, Ba, Y, Nb, Pb, and Ga were determined by XRF. A ten-gram pressed powder disk was prepared for each sample. A rhodium tube was the X-ray source and Compton scattering was used to determine the mass absorption coefficients. Working curves were established for each element using 23 well-calibrated international rock standards. Precision and accuracy are generally better than 5% for element concentrations that are three times the detection limit.

The concentrations of Sc, Co, Cs, La, Ce, Nd, Sm, Eu, Gd, Tb, Tm, Yb, Lu, Hf, Ta, Th, U, and Sb were determined by instrumental neutron activation analysis (INAA). The analyses were performed using an automated dual detector (GeLi for high-energy gamma rays and LEGe for low-energy gamma rays) system. Samples were counted 10 days after irradiation for short half-life isotopes and 2 months after irradiation for long half-life isotopes. Peak areas were determined using Canberra Instruments Spectran-AT software and final processing (decay corrections, gamma ray interferences, geometry and fluence corrections) was performed using in-house software. AGV-1 was the irradiation standard. Analytical precision for trace elements and rare earth elements (REEs) is generally better than 5%.

5. Results

The analytical data obtained in this study are reported in Supplemental Table S2 (mineral chemistry) and Table S3 (whole-rock chemistry). Also included in Table S3 are previously published data for the AAP. Data sources are listed in Table S3.

5.1. Mineral Chemistry

5.1.1. Olivine

Olivine occurs in the Prairie Creek lamproite [33] and in the Granite Mountain Ol-bearing syenite. The Prairie Creek olivines range between Fo_{90} and Fo_{92} and Granite Mountain olivines range between Fo_{65} and Fo_{71}. The Granite Mountain olivines are much richer in Mg than would be expected for olivines in syenite which are usually Fe-rich. Olivine calculations were performed with MinPlotX [49]

5.1.2. Pyroxene

Pyroxenes are found in most of the rocks in the AAP. The lamproite, carbonatite, and lamprophyre pyroxenes plot in the diopside field (Figure 9). The most Mg-rich pyroxenes are from the Prairie Creek lamproite.

The pyroxenes in the Magnet Cove garnet-nepheline syenite trend from the diopside to the aegirine-augite field. The pyroxenes from the Diamond Joe quarry in Magnet Cove are mostly iron-rich, but with relatively low alkali contents. The pyroxenes found in the Magnet Cove ijolites also plot in the diopside field. The pyroxenes from the Magnet

Cove nepheline syenite are aegirine-augite and aegirines. Six separate pyroxene trends have been identified at Magnet Cove [22].

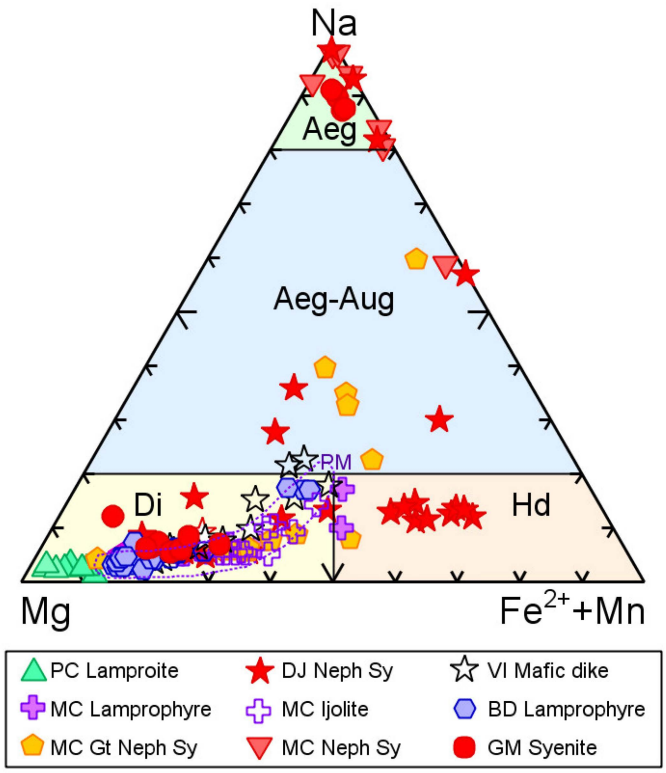

Figure 9. AAP pyroxene compositions plotted in the Mg-Na-Fe^{2+} + Mn diagram [19]. The field labeled PM is the chemistry of pyroxenes from the Perryville–Morrilton carbonatite [35]. Some of the Magnet Cove nepheline syenite pyroxene compositions are from Flohr and Ross [22]. PC—Prairie Creek, MC—Magnet Cove, DJ—Diamond Joe quarry, Magnet Cove, VI—V-Intrusive, BD—Benton dike swarm, and GM—Granite Mountain. Pyroxene calculations performed using MinPlotX [49].

Two distinct pyroxene compositions are found in the Granite Mountain syenites. The pyroxenes from the olivine-bearing syenite are diopsides while those from the pegmatitic syenite are aegirines.

5.1.3. Amphibole

Amphiboles are classified using the most recent IMA classification scheme (Figure 10, [50]). Amphiboles from the Perryville–Morrilton carbonatite are tschermakites. Amphiboles from the Magnet Cove nepheline syenite and phonolite are tschermakites and ferro-tschermakites, reflecting a change in the Fe-Mg content of the amphiboles. The Magnet Cove garnet-nepheline syenite amphiboles are tschermakites. The Magnet Cove lamprophyre dike amphiboles are ferro-tschermakites. The amphiboles from the Benton camptonite are tschermakites while those from the Benton felsic dike are tschermakite and ferro-tschermakites. The amphiboles from the Ol-bearing syenites from Granite Mountain are classified as tschermakite, magnesio-hornblende, ferro-glaucophane, and riebecite. Unlike the olivines and pyroxenes, some of the amphiboles in the olivine-bearing syenite are iron- and alkali-enriched. The amphiboles from the Granite Mountain pegmatitic syenite are riebeckites and magnesio-riebeckites, reflecting a significant enrichment in iron and alkalis in this lithology. Chlorine is at or below detection in all samples. Fluorine is a significant component of the hydroxyl site, ranging up to 70% in some of the Granite Mountain syenites.

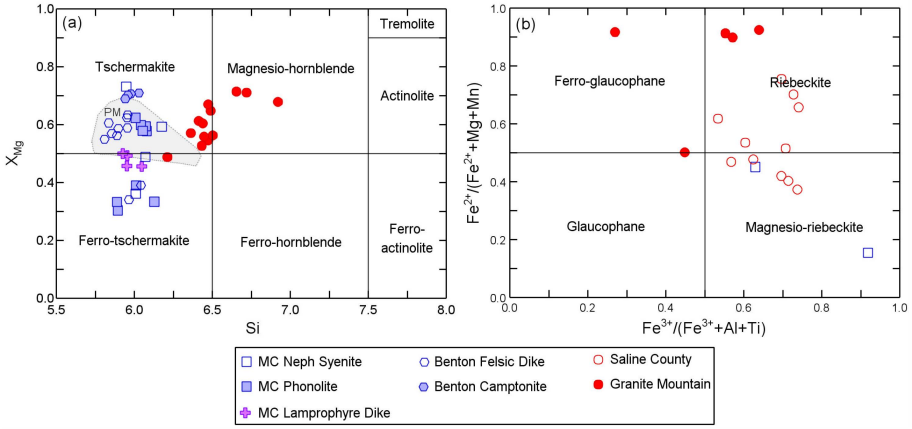

Figure 10. (**a**,**b**). AAP amphibole nomenclature based on the most recent IMA classification [50]. Field labeled PM in panel (**a**) is the composition range for amphiboles from the Perryville–Morrilton carbonatite [35]. Amphibole classification performed using MinPlotX [49].

5.1.4. Micas

Micas range in composition from almost end-member phlogopite to end-member annite (Figure 11). Lamproite and carbonatite micas plot in the phlogopite field as do some micas from the Magnet Cove ijolites and Benton lamprophyres. As was the case for the olivines, pyroxenes, and amphiboles, the Granite Mountain micas are Mg-rich biotites. The micas from the nepheline syenites at Magnet Cove are iron-rich (Figure 11a). Micas from the lamproites, Benton lamprophyres, and Granite Mountain are enriched in titanium relative to the micas from other lithologies (Figure 11b). A manganese enrichment trend, with increasing Fe/Fe + Mg ratio, is observed for the Granite Mountain micas. Some of the micas from the Magnet Cove nepheline syenites show a strong relative enrichment in Mn. As was the case for the amphiboles, Cl is generally below detection and F is the major halogen in the hydroxyl site. However, unlike the amphiboles, in all cases hydroxyl ions are the dominant species in this site. Crystallization temperatures were calculated using a machine learning approach [51] and the results are reported in Table S2.

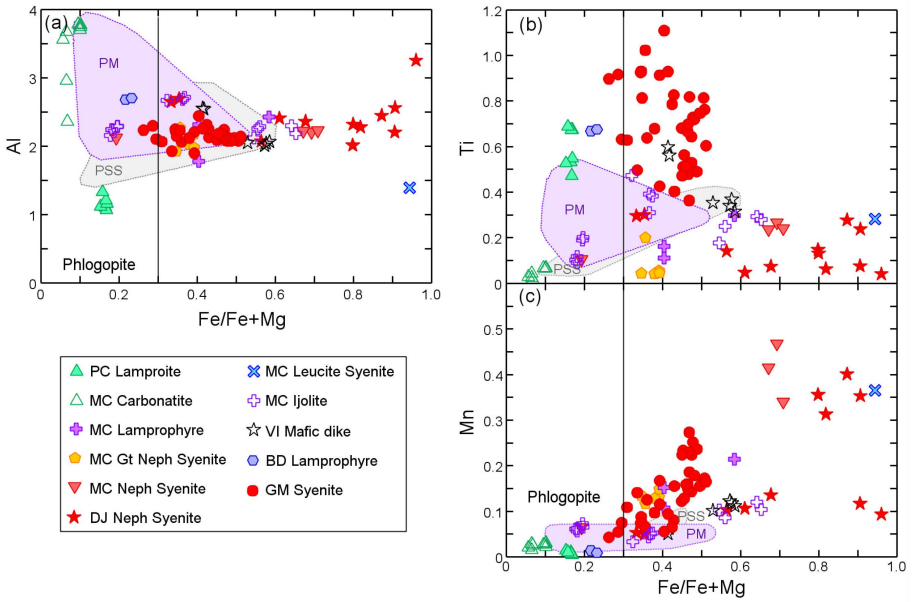

Figure 11. AAP mica compositions. (**a**) Al versus the Fe/Fe + Mg ratio. (**b**) Ti versus the Fe/Fe + Mg ratio. (**c**) Mn versus Fe/Fe + Mg ratio. PM—micas from Perryville–Morillton carbonatite [35]. PSS—micas from Potash Sulphur Springs carbonatite and silicate rocks [25]. Mica formula calculated on the basis of 22 oxygens and all Fe as Fe^{2+}. Water content calculated using the method of [52].

5.1.5. Astrophyllite Group Minerals

Astrophyllite and kupletskite occur in the silica undersaturated medium-grained syenite and pegmatitic syenite at the "Bath" quarry in Saline County. Astrophyllite group minerals, compared to phlogopites and biotites, are favored in magmas with mol[$(Na_2O + K_2O)/Al_2O_3$] > 1, high Ti + Fe, and high F/Cl ratios [53]. Note that, in Table S2, the total oxides for this mineral are ~92%. Nb and Zr, which are major components of the astophyllite group minerals, were not measured in this study. The composition (Figure 12) varies from Fe-rich (astrophyllite in medium-grained syenite) to Mn-rich (kupletskite in pegmatitic syenite). Fluorine contents vary between 1.20 and 1.99 wt.%. Astrophyllite group minerals found in silica-undersaturated rocks show a wider range of Fe and Mn contents than those found in silica-saturated rocks (which tend to be Fe-rich). The increase in Mn content, relative to Fe, is ascribed to increasing redox conditions [53], which implies that crystallization of the pegmatitic phase occurred under more oxidizing conditions.

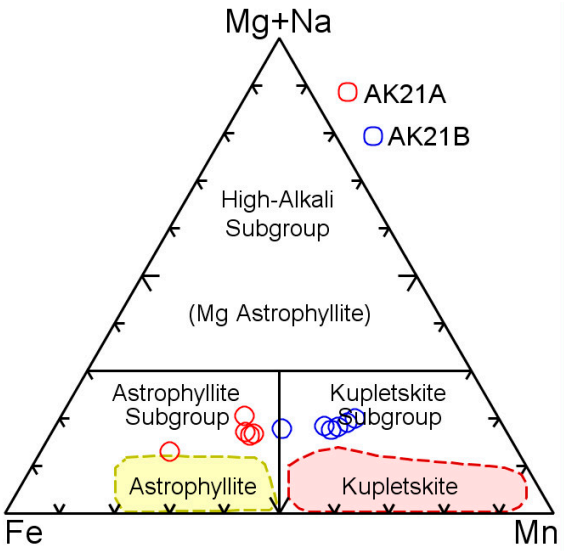

Figure 12. Astrophyllite group minerals classification diagram [53]. The Granite Mountain syenite astrophyllite group mineral (AK21A) plots in the astrophyllite field while the pegmatite astrophyllite group mineral (AK21B) plots in the kupletskite field. Colored fields encompass the range of compositions reported in [53]. Astrophyllite calculations performed with MinPlotX [49].

5.1.6. Feldspar

Feldspar compositions range form orthoclase to andesine (Figure 13a). The feldspar in the Magnet Cove phonolite is anorthoclase and andesine. The feldspar in the Magnet Cove syenites is orthoclase. The Magnet Cove lamprophyre dike has both orthoclase and anorthoclase. The Benton felsic and lamprophyric dikes both contain orthoclase and andesine. The Granite Mountain syenite feldspars range from orthoclase to andesine. The dashed lines in the figure connect coexisting minerals in a sample.

Feldspar chemistry in relation to feldspar solvi [54] is shown in Figure 13b. Dashed and solid lines connect coexisting minerals. Feldspar temperatures for the Magnet Cove syenites are between 700 °C and 800 °C. Feldspars from the Benton lamprophyre and felsic dikes range between 800 °C and 900 °C. Feldspars from the Granite Mountain syenites show a wide range of temperatures from 700 °C to 900 °C.

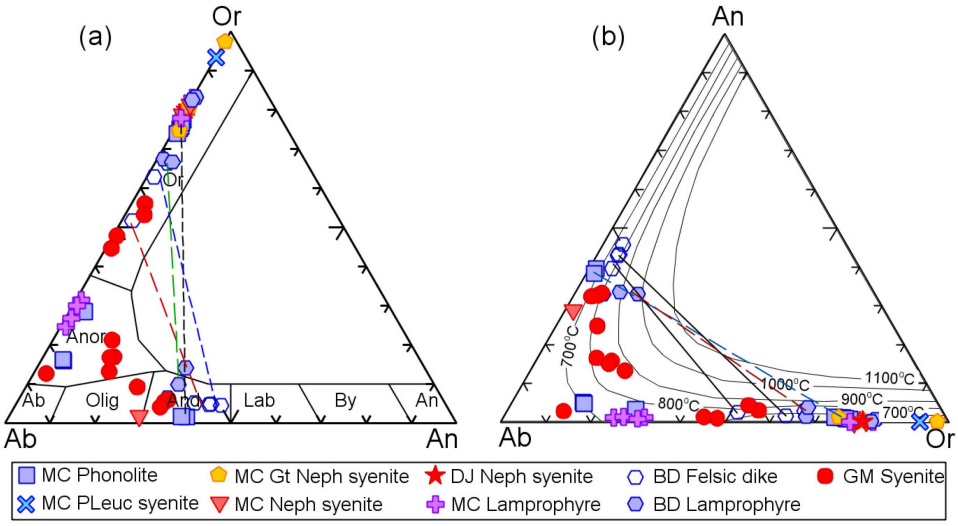

Figure 13. (**a**) Feldspar classification using Igpet 2013. (**b**) Projection of feldspar chemistries into the Ab-An-Or ternary diagram. Dashed and solid lines connect coexisting minerals. Feldspar end-members calculated using MinPlotX [49]. Feldspar solvi are from [54].

5.1.7. Nepheline

Nepheline analyses plotted in Figure 14 show a range of equilibration temperatures. The Magnet Cove nephelines from the garnet nepheline syenite, the nepheline syenite, and the ijolite mainly plot between 700 °C and 775 °C. Some of the nephelines from the Magnet Cove ijolites plot below the 500 °C isotherm, presumably due to post-magmatic re-equilibration. The nephelines from the V-intrusive mafic dike also plot between 700 °C and 775 °C. One nepheline from the V-intrusive felsic dike has an equilibration temperature of ~1000 °C.

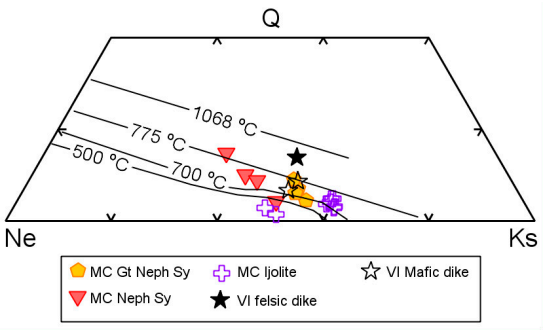

Figure 14. Nepheline analyses plotted in the expanded nepheline corner of the Neph-Qtz-Kal 1 bar phase diagram showing nepheline isotherms [55]. End-members calculated using the method of [56].

5.1.8. Garnet

Ti-rich garnets occur in the Magnet Cove nepheline syenites and ijolites. The garnets are brown to deep red in color and some have clear or pale yellow low-Ti overgrowths. Silica and Ti show a negative correlation (Figure 15a) which supports the inference that Ti substitutes for Si in the tetrahedral site [57]. The same correlation is observed for a more extensive garnet data base [57]. The TiO_2 content of the pale yellow to colorless rims varies from ~1 wt.% to 6 wt.% (Figure 15b) and is similar to that of the Somma-Vesuvius garnets which crystallized from phonolite-trachyte magmas. The low-Ti rims support the inference that ilmenite (or another Ti-containing phase) began to crystallize towards the end of garnet crystallization. The crystallization of this Ti-rich phase depleted the melt in Ti. Garnets from the nepheline syenites and ijolites show a similar range in Ti content reaching TiO_2 = 19 wt.%. The very high Ti contents are typical of melanite (a black high-Ti variety of

andradite). Compared to previous studies on Oldoinyo Lengai lavas [58] and ijolites from the Oka carbonatite complex [57], the Magnet Cove garnets encompass the entire range of reported Ti contents. In terms of Al content, most of the Magnet Cove garnets plot between the Oldoinyo Lengai and Oka fields (Figure 15c). The low-Ti garnet rims have similar Al content to the Somma-Vesuvius garnets.

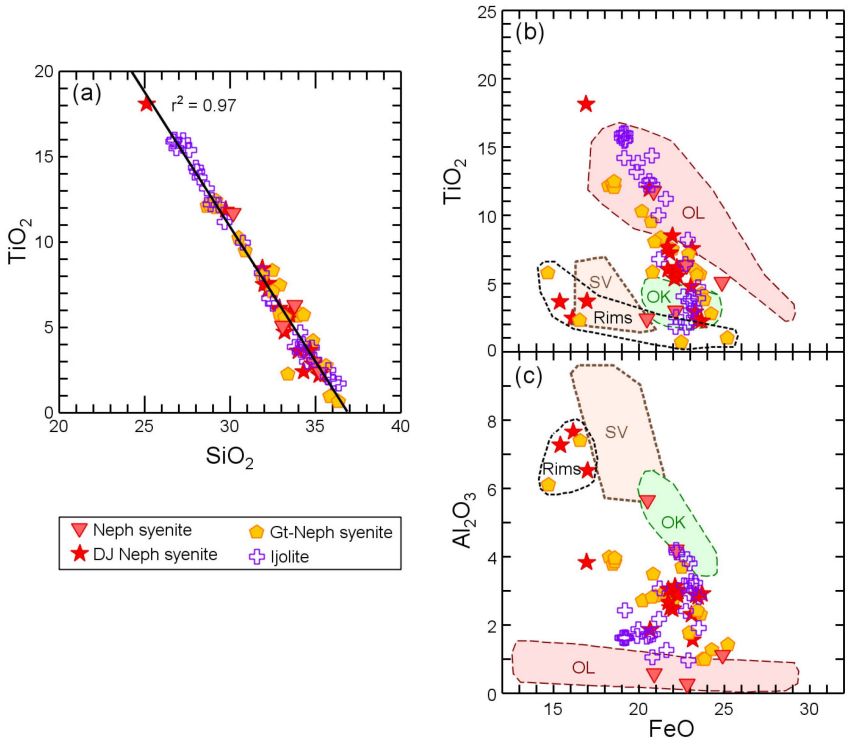

Figure 15. Garnet chemistry plots. (**a**) TiO_2 versus SiO_2. The negative correlation indicates that Ti substitutes for Si in the tetrahedral site. (**b**) TiO_2 versus FeO. The pale to colorless garnet rims have lower Ti content than the brown to dark red garnets and the compositions are similar to those of the Somma-Vesuvius garnets. The variations in Ti content cover the range of compositions reported in the literature. (**c**) Al_2O_3 versus FeO. The Al content of the Magnet Cove garnets plots between that of Oka (OK) and Ol Doinyo Lengai (OL). The garnet rims plot close to the garnets from Somma-Vesuvius and within the cluster of compositions found just above the OL field. Data sources: Oldoinyo Lengai [58], Somma-Vesuvius (SV) [59], and Oka [57]. Because of their high Ti content, apfu was calculated using Dexter Perkin's garnet calculation spreadsheet found on the *On the Cutting Edge* website (https://serc.carleton.edu/research_education/equilibria/mineralformulaerecalculation.html, accessed on 23 June 2025).

5.1.9. Titanite

Titanite compositions have been obtained for various silicate rock units from Magnet Cove, felsic and mafic dikes from the V-intrusive, and nepheline syenites from the Granite Mountain complex. In the titanite crystal structure, Al, Fe, and Mg substitute into the octahedral site occupied by Ti, and charge balance is achieved by the substitution of F and/or OH^- into the O1 site (occupied by an underbonded oxygen ion) [60]. These substitutions are illustrated in Figure 16a,b, and the linear trends support the substitution model. Titanite from the Magnet Cove phonolite is F-rich compared to most of the other titanites, which may imply crystallization of the titanite from a F-rich melt. The AAP titanites plot within the global field for the titanite chemistry of silicon-undersaturated alkaline rocks (Figure 16c,d) [60], with the exception of the Magnet Cove phonolite titanites.

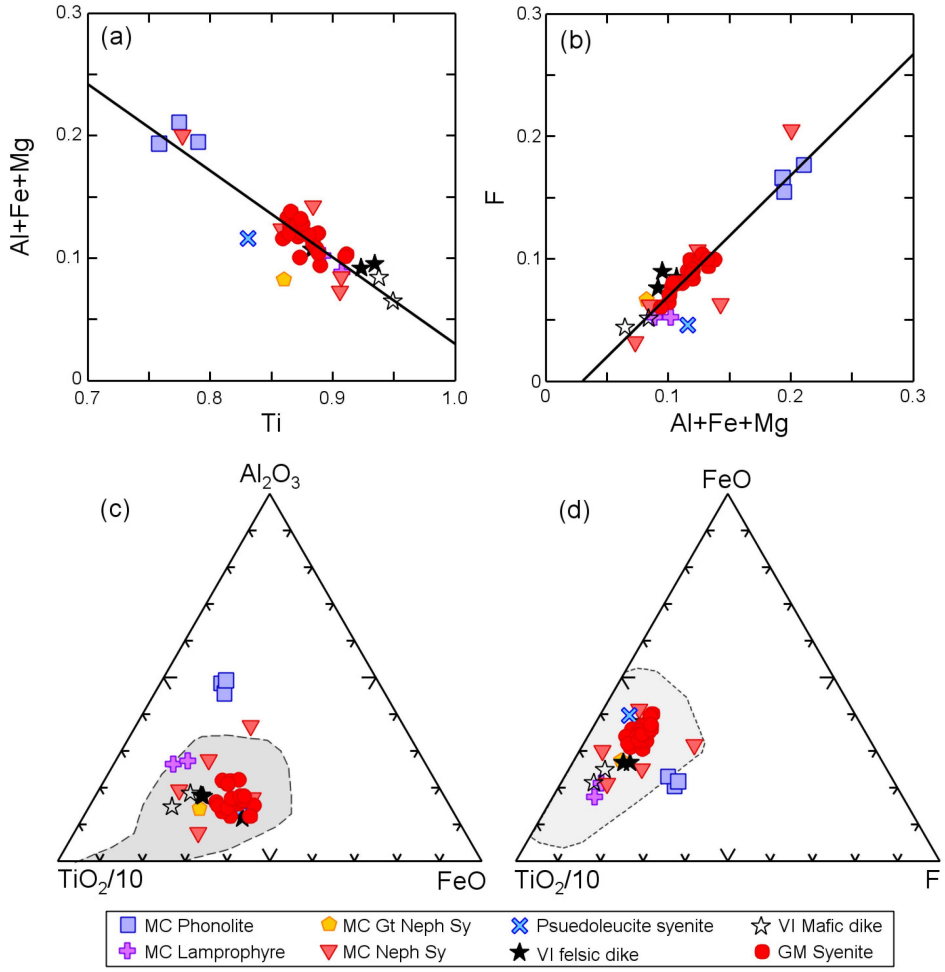

Figure 16. Titanite chemistry plots. (**a**) Linear correlation of Al + Fe + Mg vs. Ti (r^2 = 0.80) and (**b**) linear correlation of F versus Al + Fe + Mg (r^2 = 0.84). Titanite chemistry (wt.%) plotted in ternary diagrams, (**c**) TiO_2/10-Al_2O_3-FeO and (**d**) TiO_2/10-FeO-F. The gray fields represent the composition range for titanites from silica-undersaturated rocks [60]. Titanite calculations performed using MinPlotX [49].

5.1.10. Apatite

Apatite chemistry for various lithologic units from the AAP is plotted in terms of mole fractions in Figure 17. For the silicate rocks XF > 0.5 and the apatites are fluorapatites. Relative to apatites from the silicate rocks, the apatites from the Magnet Cove carbonatite have XF < 0.5 and are hydroxyapatites. As was the case for the amphiboles and micas, Cl is at or near the detection limit with the exception of apatites from a felsic dike at Benton and some apatites from the Granite Mountain syenite. Note the expanded scale for XCl which is used to show the minor enrichment of Cl in the apatites. The conclusion is that, during the crystallization of the amphiboles, micas, and apatites, Cl was not a significant component of the magmas. However, the presence of sodalite and late-stage metasomatism does indicate that the magmas did evolve Cl-rich solutions (discussed later).

The equation of [61] can be used to calculate the concentration of F in the magma from which the apatites crystallized. These values are given in Table S2. For the Magnet Cove silicate magmas, calculated F = 0.19 wt.% (phonolite), 0.18 to 0.24 wt.% (nepheline syenites), 0.14–0.21 wt.% (ijolites), and 0.19 wt.% (lamprophyre). For the V-intrusive magmas, calculated F = 0.16 wt.% (felsic dike) and 0.23 wt.% (mafic dike). For the Benton felsic dikes, calculated F = 0.17 wt.%. For Granite Mountain, calculated F = 0.19 to 0.23 wt.%.

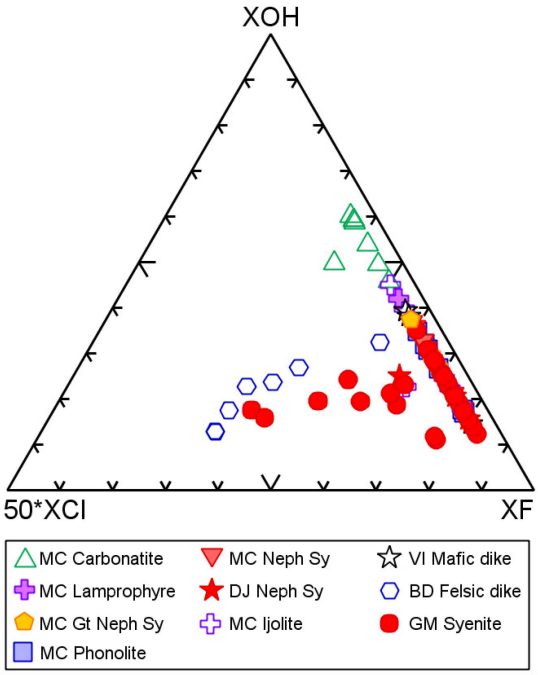

Figure 17. Apatite compositions plotted in terms of mole fractions of Cl, OH, and F. Note expanded scale for XCl in order to show the minor enrichment in Cl for some apatite samples. Mole fractions calculated using the method of [62].

5.1.11. Oxides

The major oxide mineral found in the Prairie Creek lamproite is Cr-spinel, which is a characteristic mineral for lamproites (Figure 18a,b). The common oxide minerals in the other AAP intrusions are ilmenite and magnet (Figure 18c). Chromite is found in the Magnet Cove phonolite, but is distinguished from the chromite in the Prairie Creek lamproite by its higher Cr content and lower Fe and Ti content. Coexisting ilmenites and magnetites are found at Granite Mountain and it is possible to calculate the fugacity of the melt when these minerals equilibrated [63]. The calculated values fall between the QFM and titanite buffers (Figure 18d).

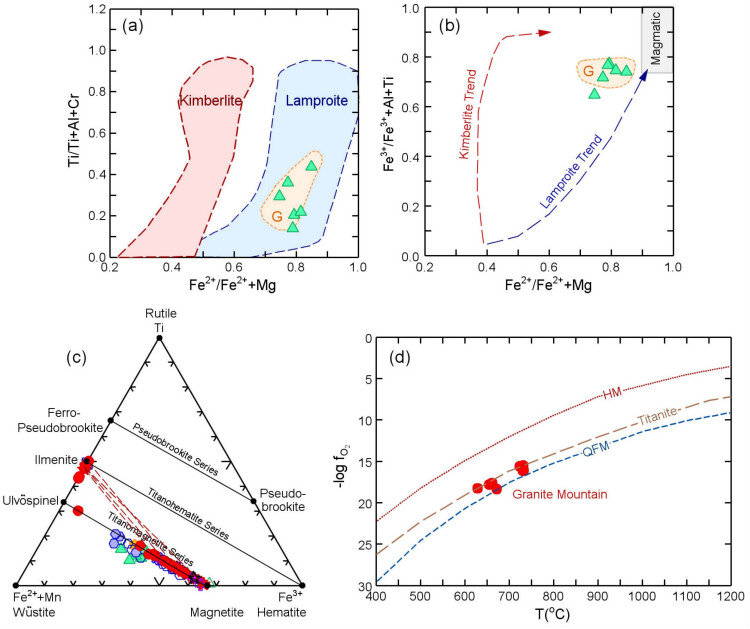

Figure 18. Oxide mineral plots for Prairie Creek and Granite Mountain. Spinels from the Prairie Creek lamproite plot in the (**a**) lamproite field and on the (**b**) lamproite trend [64–66]. Field labeled

"G" encompasses previous spinel analyses [37]. Spinel calculations performed using MinPlotX [49]. (**c**) Oxides from AAP plotted in the Fe^{2+}-Ti-Fe^{3+} mineral diagram. The magnetites show a range of compositions and the oxides from the Benton lamprophyres plot towards the ulvöspinel end of the magnetite–ulvöspinel series. The dashed red lines connect the magnetite–ilmenite pairs used for the oxygen fugacity calculation. (**d**) Calculated oxygen fugacity for Granite Mountain magnetite–ilmenite pairs [63]. Sources for buffer curves: QFM [67], Titanite [68], and HM [69].

5.2. Whole-Rock Chemistry

5.2.1. Carbonatites

Whole-rock chemistry is available for carbonatite intrusive bodies and dikes found at Magnet Cove, Potash Sulphur Springs, and Benton. The data summarized here is from the results of this study and USGS Open File Reports [26,30,47].

The bulk of the carbonatites are classified as calciocarbonatite or magnesocarbonatite (Figure 19). A few of the samples plot in the ferrocarbonatite field. With a few exceptions, for both Magnet Cove and Benton carbonatites, there is a trend towards more Mg-rich compositions. The Potash Sulphur Springs samples plot in the calciocarbonatite field with a few falling in the ferrocarbonatite field.

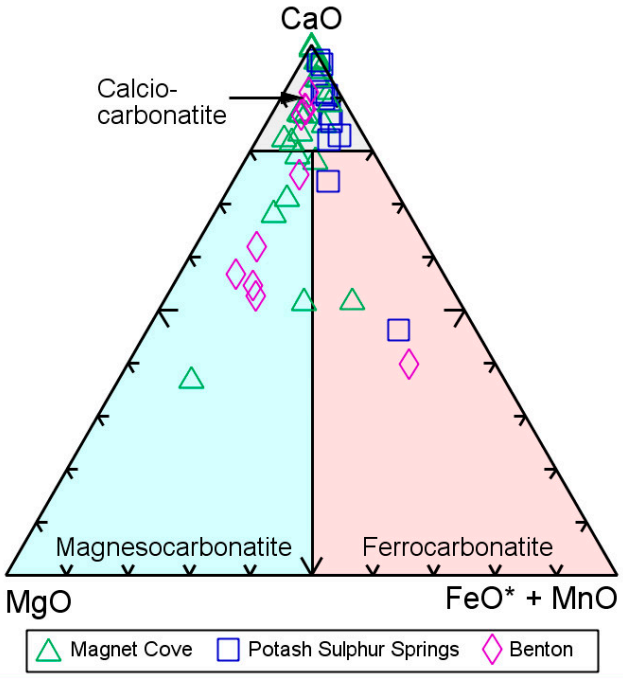

Figure 19. Classification of AAP carbonatites on the basis of weight percent oxides [70].

Chondrite-normalized REE plots and primitive-mantle-normalized spider diagrams are shown in Figure 20. The carbonatites are significantly enriched in light rare earths (LREEs) relative to heavy rare earths (HREEs). For Magnet Cove $(La/Yb)_N$ ratios vary from 6–269, for Potash Sulphur Springs from 11–153, and for Benton carbonatite dikes from 17–2879. The very high $(La/Yb)_N$ for one of the Benton carbonatite dikes is an anomaly. The next highest ratio is 294.

On the primitive-mantle-normalized diagrams all the carbonatite samples show relative depletions in Ta, K, P, Zr, and Ti. As expected in all the diagrams there is a relative enrichment in La and Ce, and Ba usually shows relative enrichment. For the other elements plotted in the spider diagrams, the observed relative abundances fit a general pattern of declining relative abundances moving from left to right on the diagrams. The conclusions to be drawn from the spider diagrams are that the relative depletion in Ta and Ti imply

removal of ilmenite, the relative depletion in Zr implies the removal of zircon, and the relative depletion in P implies the removal of apatite.

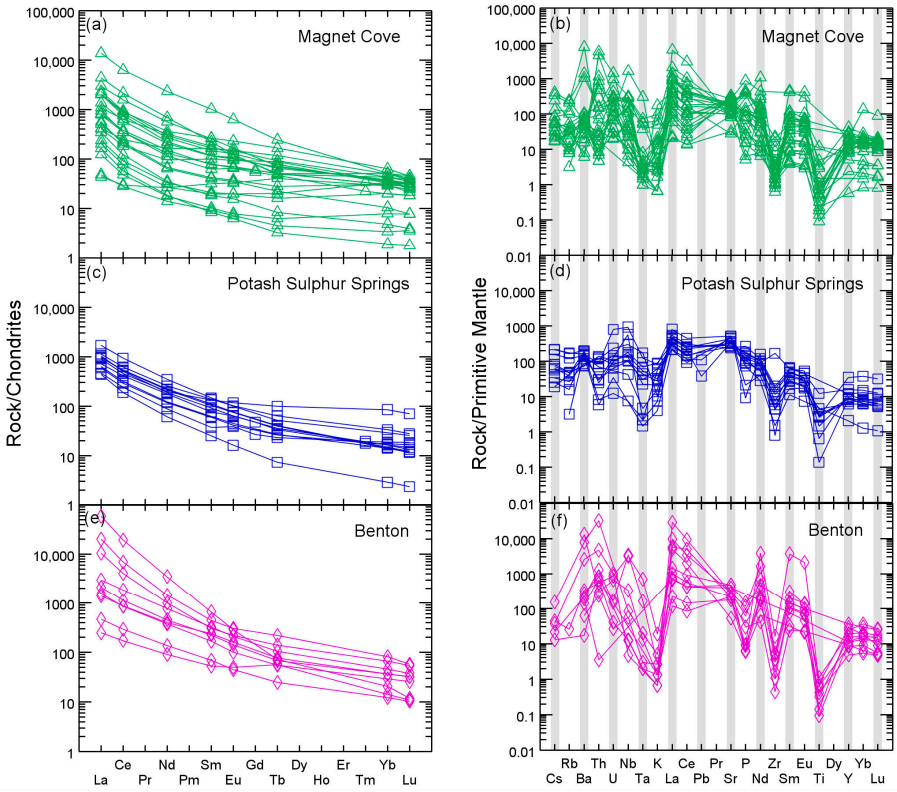

Figure 20. Chondrite-normalized REE plots and primitive-mantle-normalized spider diagrams for (**a**,**b**) Magnet Cove, (**c**,**d**) Potash Sulphur Springs, and (**e**,**f**) Benton carbonatites. Chondrite normalization values from [71] and Primitive Mantle normalization values from [72].

The relationships between elemental concentrations and various elemental ratios are shown on Figure 21. For comparison, also shown on the diagrams is the compositional range for lavas from the extrusive Fort Portal, Uganda, carbonatite [73]. Two distinct trends, with the exception of a few samples, are evident on the FeO versus MgO plot (Figure 21a). For both Potash Sulphur Springs and the Benton carbonatite dikes there is an increase in MgO with increasing FeO_T. The slope of this trend is much steeper for the Benton carbonatite dikes. The Magnet Cove carbonatites follow a trend similar to that for Potash Sulphur Springs but with significant scatter. For all three localities there is an increase in MgO with increasing SiO_2 (Figure 21b). Also shown on the diagram are mixing lines for pure $CaCO_3$ carbonatite and phlogopite (composition from phlogopite in the Magnet Cove carbonatite) and pure $CaCO_3$ carbonatite and diopside (composition from diopside in Magnet Cove ijolite). The samples from Magnet Cove tend to fall along the phlogopite mixing line, suggesting that the abundance of phlogopite in the carbonatite is the major control on MgO. Similarly, the Potash Sulphur Springs samples fall along the diopside mixing line. The trend for the Benton dike swarm is steeper and the MgO content is not controlled by a silicate mineral. For the Benton dike swarm, the MgO is most likely contained in a carbonate phase (dolomite). For the Magnet Cove and Potash Sulphur Springs carbonatites there is a regular decrease in CaO with increasing SiO_2 (Figure 21c). Note that the Benton dike swarm does not follow this trend. On the Ce versus P_2O_5 plot, for Magnet Cove and Potash Sulphur Springs there is a regular increase in Ce with increasing P_2O_5 which implies that apatite is a significant reservoir for the REEs (Figure 21d). The Benton carbonatite dike samples plot in a broad field above the Ce versus P_2O_5 trend. The Sr/Ba vs. sum REE plot (Figure 21e) shows a decrease in total REE with

increasing Sr/Ba ratio for the Benton carbonatite dikes and more generally for the Magnet Cove carbonatites. The Potash Sulphur Springs samples form a field that lies on the overall trend. On the Zr/Hf versus Th/U plot (Figure 21f) there is a regular increase in both ratios for the Potash Sulphur Springs samples. The Magnet Cove samples are scattered across the diagram and the Benton carbonatite dikes form a field that falls below the Potash Sulphur Springs trend.

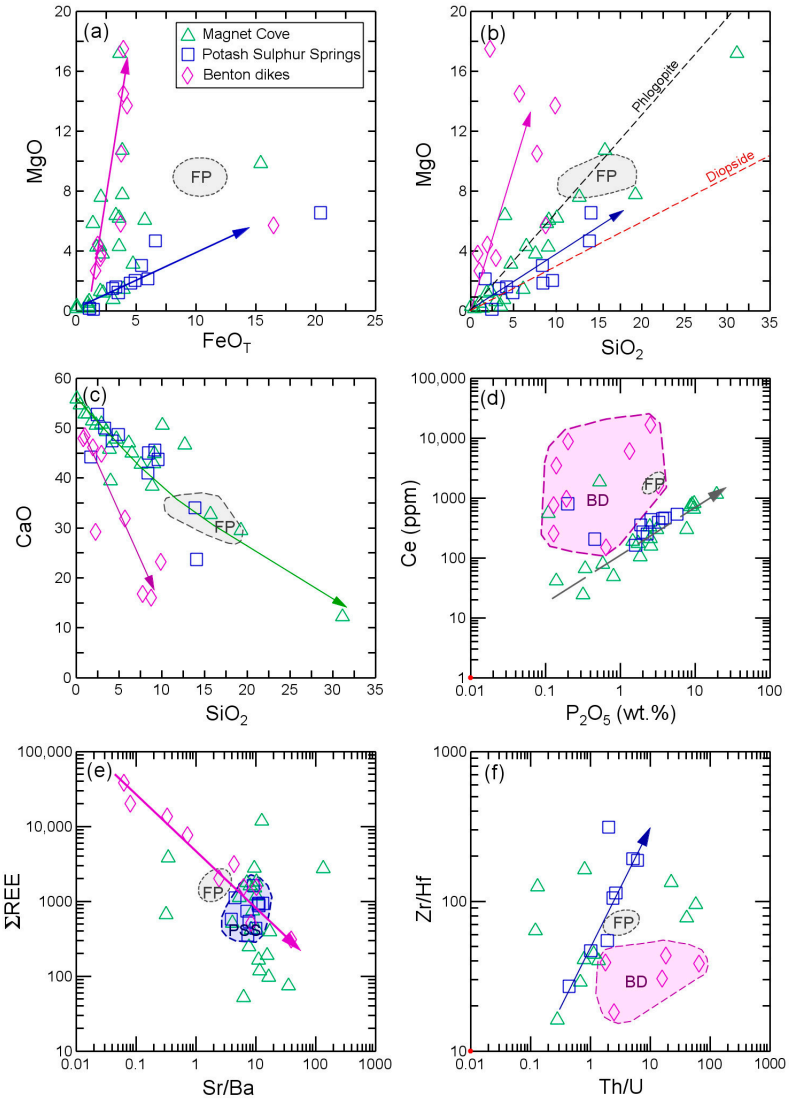

Figure 21. (**a**) MgO versus total Fe as FeO, (**b**) MgO versus SiO_2, (**c**) CaO versus SiO_2, (**d**) logarithmic plot of Ce versus P_2O_5, (**e**) logarithmic plot of total REE versus Sr/Ba ratio, and (**f**) logarithmic plot Zr/Hf versus Th/U ratios. The gray field labeled FP encompasses the range of compositions for carbonatite lavas from Fort Portal, Uganda [73]. PSS field is Potash Sulphur Springs and BD field is Benton Dikes.

5.2.2. Silicate Rocks

The fine-grained silicate rocks mostly plot in the basanite and various phonolite fields on the TAS diagram (Figure 22a). The plutonic rocks mostly plot in the foidolite and foid syenite fields on the plutonic rock classification diagram (Figure 22b). With a few exceptions, all the rocks plot in silica-undersaturated fields.

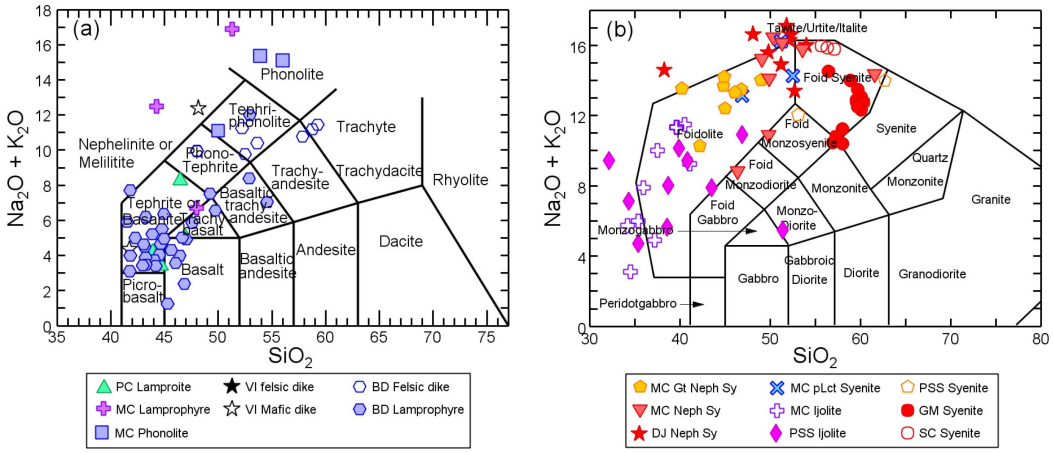

Figure 22. (**a**) Prairie Creek lamproite and fine-grained dike rocks plotted on the TAS diagram [74], (**b**) coarse-grained plutonic rocks plotted on the plutonic rock classification diagram [75].

The compositions of the volcanic and plutonic rocks are plotted on an AFM diagram (Figure 23). The compositions of the plutonic nepheline syenites (Figure 23, gray field) show the same range as their volcanic equivalents. The lamproites form a distance field characterized by high MgO concentrations and low to intermediate alkali contents. The Dare Mine Knob lamproite has distinctly higher alkali content than the lamproites from Prairie Creek.

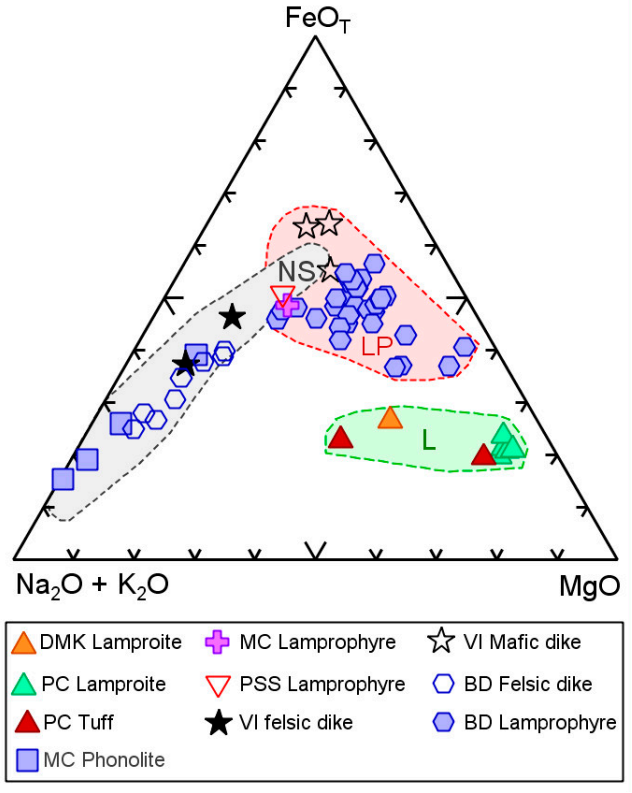

Figure 23. Alkali–total iron–Mg (AFM) diagram for AAP silicate rocks. The gray field, labeled NS, encompasses the range of compositions for the nepheline syenites (and their mineralogical variants) from Magnet Cove, Potash Sulphur Springs, Benton dike swarm, Granite Mountain, and Saline County. The lamproites (field labeled L) are chemically distinct from the lamprophyres (field labeled LP).

Chondrite-normalized REE plots and primitive-mantle-normalized spider diagrams for the lamproites, lamprophyres, and felsic dike rocks are shown in Figure 24. The REE

patterns for the lamproites show a steeper negative slope [$(La/Yb)_N$ = 110 to 135] than the REE patterns for the lamprophyres [$(La/Yb)_N$ = 15 to 37] (Figure 24a). If garnet occurs in the magma source this difference in slope is often attributed to the degree of partial melting, with the higher ratios representing smaller degrees of melting. On the primitive-mantle-normalized diagram the lamprophyres are significantly enriched in Cs compared to the lamproites (Figure 24b). Some lamprophyre samples are enriched in Ba, U, and Ta. Most samples are slightly depleted in P, suggesting apatite fractionation. For most phonolite and felsic dike samples the REE patterns are slightly concaved downwards (Figure 24c) and $(La/Yb)_N$ ratios vary, with a few exceptions, between 19 and 33. For the phonolite and felsic dike samples, on the primitive-mantle-normalized diagram (Figure 24d) samples show either enrichment or depletion in Cs, some are depleted in Th and enriched in U, and some relatively enriched in Pb and depleted in P.

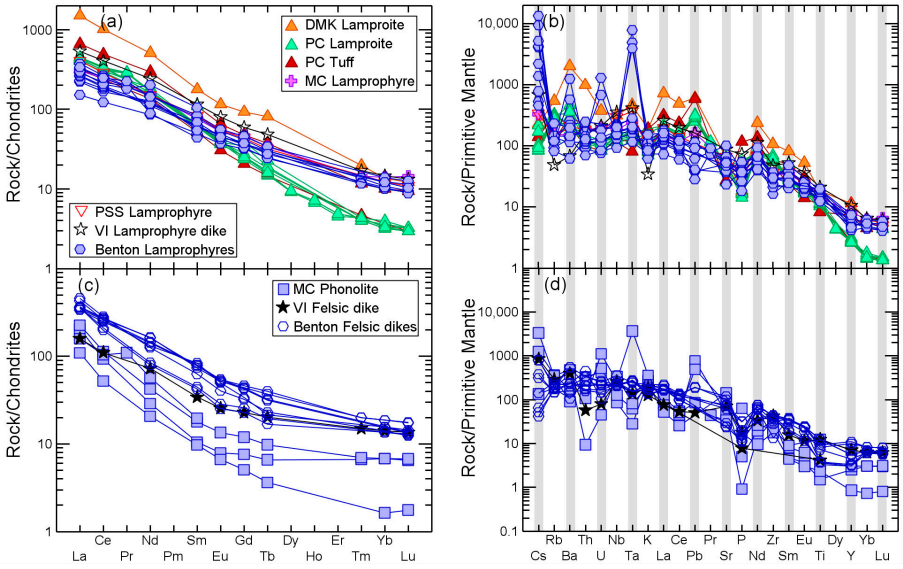

Figure 24. REE chondrite- and primitive-mantle-normalized plots for (**a**,**b**) lamproites and lamprophyres and phonolites (**c**,**d**). Chondrite normalization values from [71] and Primitive Mantle normalization values from [72].

Chondrite-normalized REE plots and primitive-mantle-normalized spider diagrams for the ijolites and various nepheline syenites are shown in Figure 25. Potash Suphur Springs ijolites have subparallel REE patterns with [$(La/Yb)_N$ = 13 to 40] while the Magnet Cove ijolites have irregular REE patterns with [$(La/Yb)_N$ = 0.4 to 74] (Figure 25a). Garnet is a common mineral in the ijolites and the HREE enrichment shown by some of the Magnet Cove ijolites may reflect the presence of cumulate garnet (garnet is enriched in HREEs) with respect to LREEs. The primitive-mantle-normalized spider diagram for the Magnet Cove ijolites also shows a great deal of variability while the Potash Sulphur Springs ijolites show similar patterns (Figure 25b). Some samples are relatively enriched in U, Ta, and Nb and relatively depleted in Ba and Th.

The various syenite sequences from Magnet Cove mostly show subparallel and slightly convex downwards REE patterns (Figure 25c). A few show small negative Eu anomalies usually associated with feldspar fractionation. The garnet-nepheline syenites tend to be relatively more HREE-enriched [$(La/Yb)_N$ = 12 to 64] compared to the other syenite sequences [(La/Yb_N) = 12 to 149]. On the primitive-mantle-normalized spider diagram (Figure 25d) the various syenite sequences tend to show relative enrichment in Ba, U, Nb, Ta, and Pb and relative depletion in Th and P. There are, however, numerous exceptions to these generalities probably reflecting the heterogeneity of the syenites caused by variable degrees of liquid-crystal mixing.

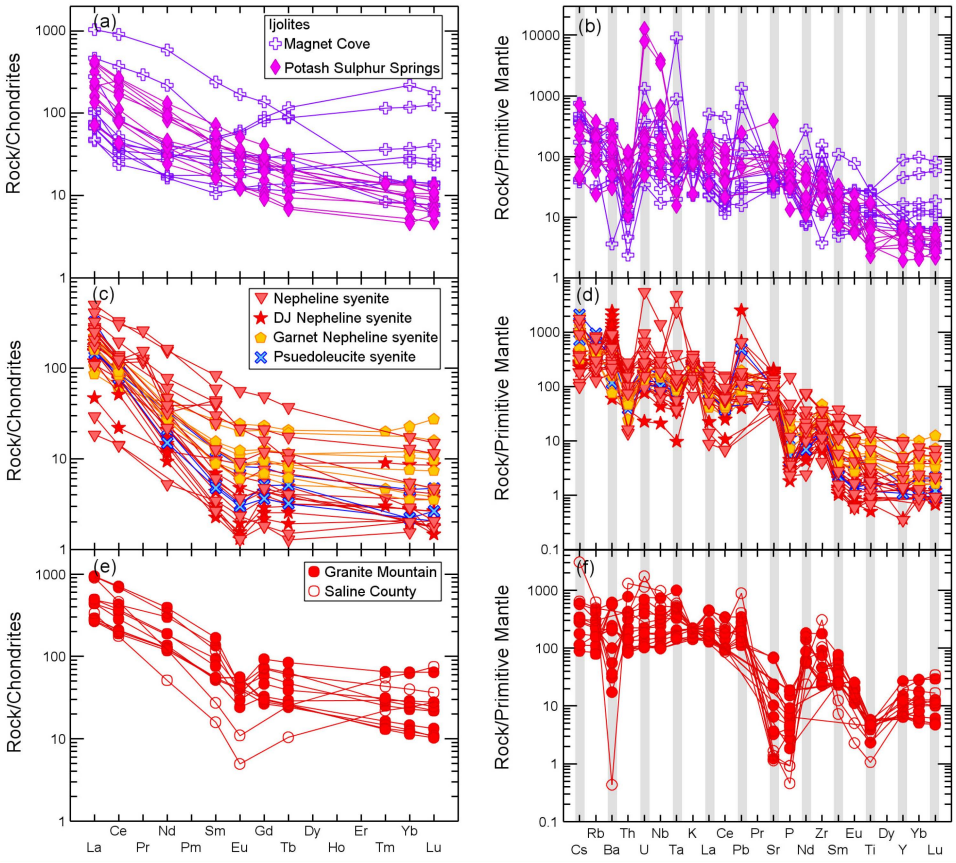

Figure 25. REE chondrite- and primitive-mantle-normalized plots for (**a**,**b**) ijolites from Magnet Cove and Potash Sulphur Springs, (**c**,**d**) Magnet Cove nepheline syenites, and (**e**,**f**) Granite Mountain and Saline County nepheline syenites. Chondrite normalization values from [71] and Primitive Mantle normalization values from [72].

The Granite Mountain nepheline syenite REE patterns are all subparallel and most show negative Eu anomalies (Figure 25e). One of the Saline County samples is similar to the Granite Mountain samples while the other two Saline County samples, which are coarse-grained to pegmatitic and come from the margin of the complex, show V-shaped patterns. On the primitive-mantle-normalized spider diagram (Figure 25f) most samples show relative depletion in Ba, Sr, P, and Ti presumably due to feldspar fractionation (Ba and Sr), apatite fractionation (P), and ilmenite fractionation (Ti).

Various elemental ratios for the lamproites and lamprophyres are plotted on Figure 26a,b. On a Zr/Hf versus Nb/Ta plot the Prairie Creek lamproites and Benton lamprophyres form distinct groups (Figure 26a) while the V-intrusive lamprophyres show a trend of increasing Zr/Hf and Nb/Ta ratios. Titanite occurs as an accessory mineral in the V-intrusive lamprophyres. For titanite the partition coefficient for Ta is approximately 4 times greater than that of Nb and the partition coefficient for Hf is approximately 3 times greater than that of Zr [76]. Fractionation of titanite from the lamprophyre melt will lead to a coupled increase in the Zr/Hf and Nb/Ta ratios. Conversely, accumulation would lead to decreases. Thus fractionation or accumulation of titanite may control these elemental ratios. The lamproites and lamprophyres show similar Nb/Ta ratios to oceanic island basalts (OIBs) but higher Zr/Hf ratios. On a Th/U versus U plot the Prairie Creek lamproites and Benton lamprophyres form distinct groups characterized by a larger Th/U ratio for the lamproites (Figure 26b). The Th/U ratio for the Benton lamprophyres is similar to that of OIBs, but the lamprophyres are enriched in U relative to OIBs.

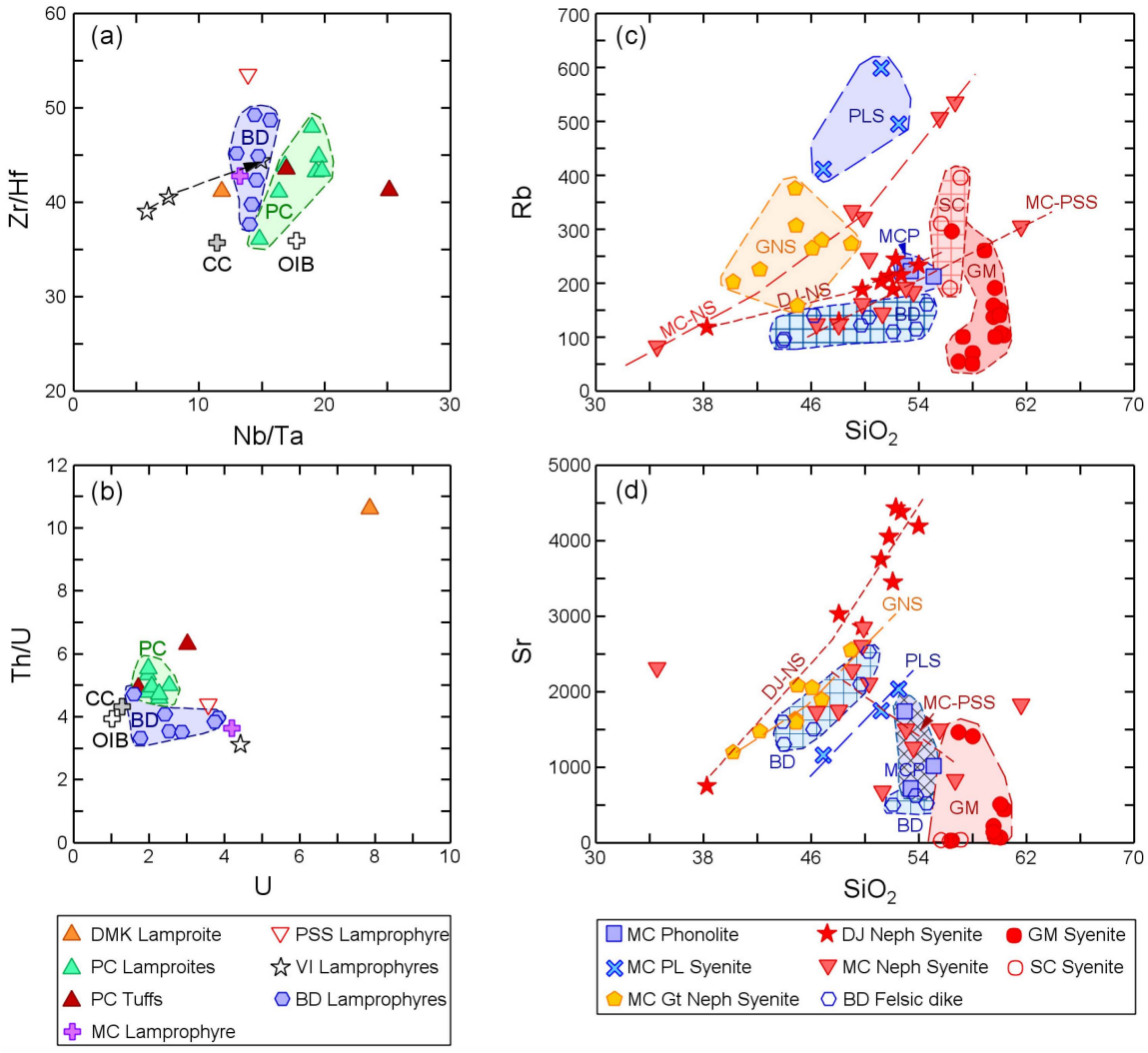

Figure 26. (**a**) Lamproite and lamprophyre compositions plotted on a Zr/Hf versus Nb/Ta diagram. CC is average continental crust [77] and OIB is average oceanic island basalt [72]. (**b**) Lamproite and lamprophyre compositions plotted on a Th/U versus U diagram. On both diagrams the lamproites from Prairie Creek and lamprophyres from Benton form distinct groups. Nepheline syenite and phonolite chemistry plotted on (**c**) Rb versus SiO_2 and (**d**) Sr versus SiO_2 diagrams. See text for discussion. Labeled fields: PC (Prairie Creek lamproite), BD (Benton lamprophyre), PLS (Magnet Cove pseudoleucite syenite), GNS (Magnet Cove garnet nepheline syenite), DJNS (Diamond Jo nepheline syenite), MC-PSS (Magnet Cove & Potash Sulphur Springs nepheline syenite), MCP (Magnet Cove phonolite), GM (Granite Mountain syenite).

Rb and Sr versus silica plots for the nepheline syenites, felsic dikes, and phonolites are shown in Figure 26c,d. On the Rb versus SiO_2 plot (Figure 26c) a number of distinct groupings and trends are seen. The Magnet Cove garnet-nepheline syenites, pseudoleucite syenites, and phonolites form distinct fields with the pseudoleucite syenites having the highest Rb content. The Benton felsic dikes also form a field with lower Rb abundances and the Saline County and Granite Mountain nepheline syenites have similar SiO_2 content but the Saline County nepheline syenites have higher Rb content. Three trends are also shown, one for the Magnet Cove nepheline syenites, one for the Diamond Joe nepheline syenites, and one that encompasses nepheline syenites from Magnet Cove and Potash Sulphur Springs. The Sr versus SiO_2 plot (Figure 26d) shows trends of increasing Sr with increasing SiO_2 for the Diamond Joe nepheline syenites, the garnet-nepheline syenites, and the pseudolecite syenites. During fractional

crystallization alkali feldspar and plagioclase would preferentially remove Sr, thus the increase in Sr with increasing SiO_2 suggests that neither of these minerals played a role in the evolution of these syenites. The Benton felsic dikes plot in an elongated field that aligns with the syenite trends, suggesting that feldspar fractionation did not play a role in the evolution of these felsic dikes. Several Benton dike swarm samples have low Sr content so that feldspar fractionation may have played a role in the chemistry of these dikes. The Magnet Cove–Potash Sulphur Springs nepheline syenites form two groups, one of which plots in the Benton dike swarm field and the other (indicated by the red dashed line in Figure 26d) which shows a decrease in Sr with increasing SiO_2. The Magnet Cove phonolites and Granite Mountain nepheline syenites form fields that are elongated in a vertical direction, suggesting possible feldspar fractionation.

Previous work on the Magnet Cove nepheline syenites [19], using pyroxene chemistry, identified a number of crystallization trends—(1) Diamond Joe nepheline syenite, (2) pseudoleucite-nepheline syenite, (3) garnet-nepheline syenite, (4) titanite (sphene)-nepheline syenite, (5) alkali syenite, and (6) miscellaneous nepheline syenites. The SiO_2 versus Rb and Sr plots also suggest multiple crystallization trends—(1) Diamond Joe nepheline syenite, (2) pseudoleucite-nepheline syenite, and (3) garnet-nepheline syenite—which match the pyroxene-defined trends. An additional trend, Magnet Cove nepheline syenites, is identified on the Rb versus SiO_2 plot.

5.2.3. F and Cl

Cl and F concentrations were determined by electron microprobe for amphibole, mica, and apatite from various lithologic units in the AAP. These data are reported in Section 5.1 Mineral Chemistry. The notable conclusion is that the dominant halogen in all these minerals is F, and Cl content is near or below detection. The exceptions are for some apatites from the Benton felsic dikes (maximum 0.16 wt.%) and Granite Mountain nepheline syenites (maximum 0.11 wt.%) (Figure 17). Sodalite does appear as a late crystallizing phase in some syenites so at some point Cl concentrations are great enough to stabilize sodalite. The calculated concentrations of F in the liquid coexisting with the apatites vary between 0.14 and 0.23 wt.%.

Fluorine and Cl abundances were not determined for the rock samples analyzed for this study. However, the U.S. Geological Survey Analytical labs routinely determined F and Cl by selective ion electrode (see Open File Reports for details) when performing whole-rock analysis. Since the mineral chemistry was studied in different samples, it is not possible to directly compare the results, but it is useful to look at the whole-rock F and Cl data for the AAP (Figure 27). With only a few exceptions, Cl content for the carbonatites is 0.2 wt.% or less. F content for the carbonatites ranges from below detection up to 15 wt.%. For all the silicate rocks F content is less than 0.6 wt.%. The Magnet Cove and Potash Sulphur Springs ijolites have Cl contents ranging between 0.02 and 0.4 wt.%. The Diamond Joe nepheline syenites are relatively enriched in Cl (sodalite is found in these rocks) and this is also the case for some Magnet Cove nepheline syenites. While the system is dominated by F, apparently late-stage liquids/fluids do become relatively enriched in Cl.

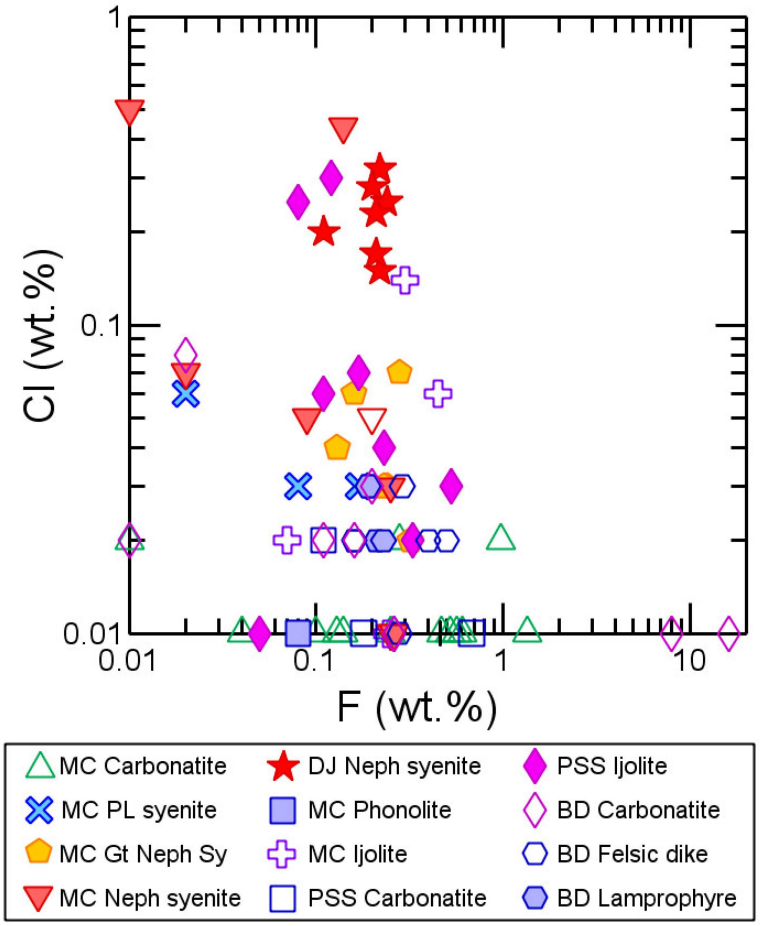

Figure 27. Cl versus F (wt.%) for carbonatites, lamprophyres, and various nepheline syenites and felsic dikes. Data from [19,22,26,30,45,47].

6. Discussion

Based on existing radiometric ages, igneous activity in the Arkansas alkaline province (AAP) extended over a period of 18 million years, from 106 Ma to 88 Ma. Lamproites emplaced at Dare Mine Knob (106 Ma) and Prairie Creek (~104 Ma) are the oldest intrusive events. Subsequently, between 100 and 98 Ma, carbonatites, phonolites, lamprophyres, and nepheline syenites are emplaced at Magnet Cove, Potash Sulphur Springs, Benton, and Perryville–Morrilton. After a hiatus of ~8 million years, nepheline syenite bodies are emplaced at Granite Mountain and Saline County (90–88 Ma). Neither carbonatites nor mafic igneous rocks are associated with the youngest period of igneous activity.

6.1. Lamproites and Lamprophyres

6.1.1. Crystallization Conditions

Lamproite and lamprophyre compositions projected into the olivine–diopside–nepheline phase diagram [78], with a few exceptions, are silica-undersaturated (Figure 28a). The lamproites plot in the olivine first field (with one exception), but note that the Dare Mine Knob (DMK2) sample plots much closer to the olivine–pyroxene cotectic. The lamprophyres plot either in the olivine first (analogous to monchiquites) or the pyroxene first (analogous to camptonites) field. A number of samples plot near or on the cotectic which suggests cocrystallization of olivine and pyroxene. The experiments on which this phase diagram is based were performed for an anhydrous system. Thus phlogopite/biotite and amphibole, two important phases in these rocks, are not represented. Thermodynamic modeling performed using Pele 7.07 [79] and Easy Melts 0.2.4-Win64 [80] software yields

similar results in that olivine or pyroxene are the first phases to crystallize. Liquidus temperatures calculated using these models are several hundred degrees too high, a reflection of the fact that the models are not calibrated for the magma chemistry encountered in this study. Temperature estimates, using a machine-learning-based biotite geothermometer [51], for the Prairie Creek lamproite are 1015 °C (AK1) and 1046 °C (AK3). A lamprophyre dike from the V-intrusive gave a calculated biotite temperature of 828 °C (AK8) and a lamprophyre dike from the Benton dike swarm gave a calculated biotite temperature of 982 °C (AK19). These temperatures support the inference that biotite would crystallize from these melts at temperatures well above the solidus.

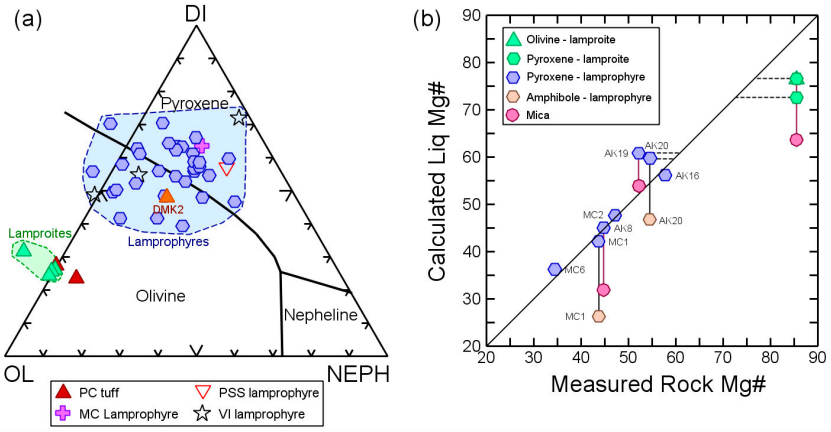

Figure 28. (**a**) Lamproite and lamprophyre compositions projected into the olivine–diopside–nepheline basalt phase diagram [78]. The lamproites fall along the Ol-Di tie-line and into the silica saturated field, but note that these are probably not liquid compositions (see text). The Dare Mine Knob (DMK2) lamproite plots in the olivine first field. A number of the lamprophyres plot on or close to the olivine–augite cotectic, indicating cocrystallization of these two minerals. Other lamprophyres plot in the olivine first (analogous to monchiquites) and pyroxene first (analogous to camptonites) fields. (**b**) Calculated Mg# of liquid versus Measured Rock Mg#. Amphibole, biotite, olivine, and pyroxene were used to calculate the liquid Mg#. See text for discussion.

It is possible to calculate the Mg# (Mg/[Fe + Mg]) for liquids coexisting with various silicate phases given the mineral/melt distribution coefficient ($Kd^{Mineral/Melt}$ = $(XFe/XMg)^{Mineral}/(XFe/XMg)^{Melt}$. These calculations were performed for four minerals found in the lamproites and lamprophyres: amphibole [81] (Kd = 0.38), biotite and phlogopite [81] (Kd = 0.31), olivine [82] (Kd = 0.31), and pyroxene [83,84] (Kd = 0.26). These Kd values were determined for mafic igneous rocks. Calculated melt Mg#s, based on the mineral chemistry, are compared to the Mg#s for the host rock (Figure 28b). If the mineral and rock values agree the inference is that the rock represents the liquid in equilibrium with the mineral at the time of crystallization. For the Prairie Creek lamproites, the melt Mg#s calculated using olivine are significantly less than the Mg#s for the whole rocks. Large olivine phenocrysts are abundant in the lamproites (Figure 3). The Mg# for the lamproites is ~86, well above that expected for magmas in equilibrium with mantle olivine. The olivine phenocrysts have Mg# ~93 and the accumulation of olivine can account for the high Mg# of the lamproites, i.e., the lamproite is essentially an olivine mush. For the Dare Mine Knob lamproite (DMK2) the Mg# is 76.9, in agreement with that expected for a primitive magma in equilibrium with mantle olivine.

The calculated pyroxene and rock Mg#s for five of the seven camptonite samples fall on the 1:1 line, i.e., the calculated melt Mg#s using pyroxene are the same as the rock Mg#s. The inference is that the pyroxene was in equilibrium with the magma (represented by the whole-rock composition) at the time of crystallization. For two of the camptonite samples (AK19, AK20) the pyroxene melt Mg#s are slightly greater than the rock Mg#s,

which suggests that these pyroxenes formed earlier in the magmatic history. For AK19, the melt Mg# calculated from the biotite composition is in agreement with the rock Mg#. Note that pyroxene and biotite are the phenocryst phases in AK19 (Figure 6). In all other instances, the calculated amphibole and biotite melt Mg#s are significantly less than the rock Mg#s, indicating that they precipitated later in the crystallization sequence.

6.1.2. Trace Elements

Because the lamproites contained significant cumulate olivine at the time of emplacement, the following discussion is confined to trace elements that have very small olivine/melt partition coefficients. The major impact of the cumulate olivine is the dilution of elemental concentrations, but the elemental ratios should not be affected. On the Th-Hf-Nb/2 classification diagram [85,86] both the lamproites and lamprophyres plot in the anorogenic field (Figure 29a). The Dare Mine Knob sample (DMK2) does not plot with the other lamproites. The lamprophyres plot close to the average alkaline lamprophyre while the lamproites plot close to the average alkaline lamproite. On the Th/Yb versus Nb/Yb tectonic discriminant diagram [87] (Figure 29b) the lamprophyres plot near average OIB while the lamproites are more enriched. Note that DMK2 falls outside the array in the direction of subduction enrichment. On the $(^{143}Nd/^{144}Nd)_I$ versus $^{147}Sm/^{144}Nd$ diagram (Figure 29c) the lamproites plot in the ancient enrichment field while the lamprophyres plot in the plume component field [88]. On the OIB source discriminant diagram (Figure 29d) the lamprophyres plot in the HIMU–EMI portion of the diagram [89], indicating a source characterized by mixing between HIMU and EMI components. On Pb (Figure 29e) and Zr/Nb (Figure 29f) versus $\varepsilon_{Nd(t)}$ plots the lamprophyres and lamproites are isotopically distinct. The lamproites have significantly higher Pb content and Dare Mine Knob has the highest Pb content. High Pb is considered indicative of a sediment input, in this case in the source region. The Zr/Nb ratios of the lamproites are a factor of two greater than those of the lamprophyres. On the basis of trace element data it is possible to identify two source regions: (1) a highly enriched depleted (probably lithospheric) mantle that was the source of the lamproite magmas and (2) a less enriched asthenospheric source region (similar to the HIMU/EM reservoirs) that was the source of the lamprophyre magmas.

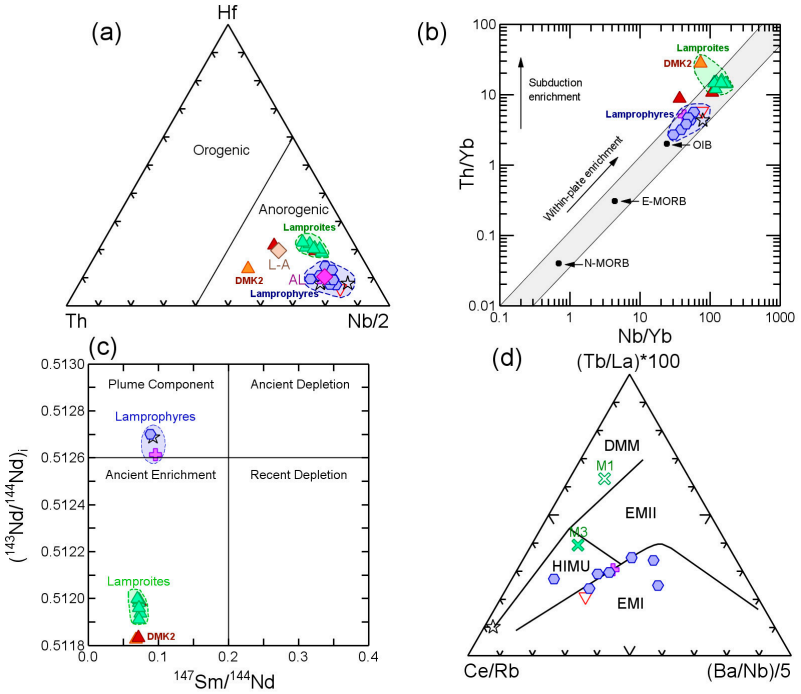

Figure 29. *Cont.*

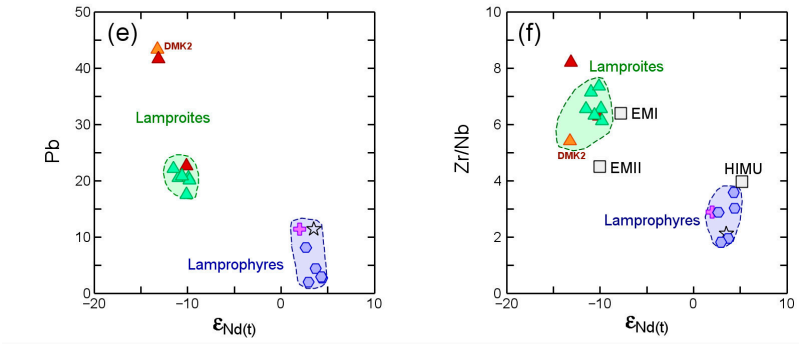

Figure 29. (**a**) Th-Hf-Nb/2 lamproite/lamprophyre classification diagram [85,86]. A-L average alkaline lamproite and AL average lamprophyre. (**b**) Th/Yb vs. Nb/Yb tectonic discriminant diagram [87]. (**c**) $(^{143}Nd/^{144}Nd)_I$ versus $^{147}Sm/^{144}Nd$. Fields from [88]. (**d**) OIB source discriminant diagram [89]. M1 and M3 are estimated mantle sources for OIB magmas [90] (**e**) Pb and (**f**) Zr/Nb versus $\varepsilon_{Nd(t)}$. Modern day $^{143}Nd/^{144}Nd$ = 0.512638. Average values of HIMU, EMI, and EMII from [91].

6.1.3. Radiogenic Isotopes

A compilation of the published radiogenic isotope data [8,43,44,46,92] can be found in Supplemental Table S3. Standard isotope plots are found in Figure 30. This section of the paper focuses on the lamproites and lamprophyres, but the isotopic data for all the lithologies is plotted in Figure 30. Several papers [8,9] have emphasized the similarity between the AAP and Monteregian Hills (MH) alkaline provinces. For comparison purposes isotopic data for the western (silica undersaturated) intrusions of the MH are included on the plots.

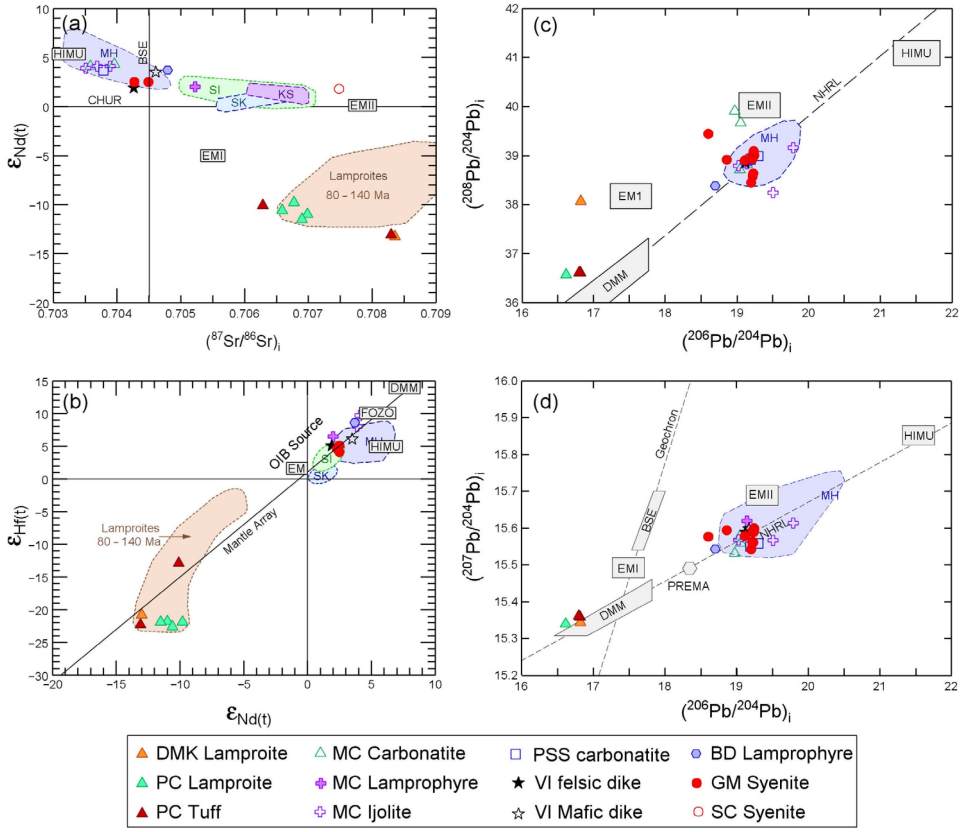

Figure 30. (**a**) $\varepsilon_{Nd(t)}$ versus initial $^{87}Sr/^{86}Sr$. MH—Monteregian Hills [93,94]. Kimberlites: SI—Somerset Island, SK—Saskatchewan, KS—Kansas [9]. Lamproite field [43]. Isotopic reservoirs DMM, PREMA, BSE, EMI, EMII, and HIMU compiled from [95,96]. (**b**) $\varepsilon_{Hf(t)}$ versus $\varepsilon_{Nd(t)}$. Mantle array and isotopic reservoirs [97,98]. (**c**,**d**) Pb isotopic diagrams.

On the Nd versus Sr isotope diagram (Figure 30a) the lamproites and lamprophyres plot in two distinct fields. A subset of the global lamproite data set [43] for samples between 80 and 140 Ma in age is shown on the diagram. The AAP lamproite samples plot within or at the very edge of this field. The AAP lamprophyres plot within the MH field, suggesting a common mantle source. Also included in the diagram are midcontinent kimberlites which formed at the same time as the AAP and have been linked to a wider period of magmatism that is inferred to have originated in the upper transition zone or in the asthenospheric mantle just above the transition zone [9]. The AAP lamprophyres plot close to the HIMU reservoir while the kimberlites and some of the other AAP lithologies lie along a trend that extends from the HIMU to EMII reservoir.

On the Hf versus Nd isotope diagram (Figure 30b) all the samples lie along, or in the case of the lamproites, just below, the mantle array. The lamproites fall in the global lamproite field. The AAP lamprophyres plot close to the HIMU reservoir and in the MH field, while the kimberlites lie along the mantle array plotting towards the EM reservoir. The kimberlites and lamprophyres plot within the region of enriched mantle sources (i.e., the OIB sources).

On the Pb isotope diagrams (Figure 30c,d) the lamproites plot near the DMM and EMI fields. On the $^{207}Pb/^{204}Pb$ versus $^{206}Pb/^{204}Pb$ diagram (Figure 30d) the Praire Creek and Dare Mine Knob samples plot in essentially the same place while on the $^{208}Pb/^{204}Pb$ versus $^{206}Pb/^{204}Pb$ diagram the Dare Mine Knob sample has a much higher initial $^{208}Pb/^{204}Pb$ ratio and plots near EMI. The Dare Mine Knob sample has a much greater Th concentration than the Prairie Creek lamproites which accounts for the larger $^{208}Pb/^{204}Pb$ ratio. The lamprophyres plot within the MH field on both diagrams and the Pb isotopic signatures for the lamprophyres are similar to that of EMII reservoir.

Nonradiogenic $\gamma Os = -3.2$ to -3.6 and $\varepsilon Nd = -10$ [46] have been obtained for the Prairie Creek lamproites. Depleted mantle model ages [46] are 1200 Ma (Nd) and 1200 and 850 Ma (Os). Other studies [8,43] report Nd-depleted mantle model ages ranging from 1200 to 1400 Ma. Hf-depleted mantle model ages are older, varying from 1600 to 1700 Ma [8]. For the lamprophyres Nd-depleted mantle model ages vary from 500 to 700 Ma [8,92] and Hf-depleted mantle model ages similarly vary from 500 to 700 Ma [8]. Thus, the isotopic data define two distinct source regions for the AAP magmas.

6.1.4. Petrogenesis of Lamproites and Lamprophyres

The elemental and isotopic data identify two distinct sources for the lamproite and lamprophyre magmas—old enriched lithospheric mantle as the source for the lamproites and an OIB-like source for the lamprophyres. The Dare Mine Knob lamproite is chemically distinct from, but isotopically similar to, the lamproites at Prairie Creek. For example, the Dare Mine Knob sample has a greater Th and U content but similar Nd and Hf isotopic ratios (Figure 30b). The isotopic similarities, but chemical differences, suggest that the Prairie Creek and Dare Mine Knob lamproites have both been extracted from a similar depleted mantle, but this mantle has undergone variable degrees of enrichment. On the various chemical discriminant and isotopic diagrams the lamprophyres plot in the OIB field and generally close to HIMU and EMI and/or EMII reservoirs (Figures 29 and 30).

Mantle xenoliths occur in the Prarie Creek lamproites, along with occasional diamonds, and approximately 40 of these xenoliths were selected for thermodynamic investigation [12]. The suite consists of dunite (20%), harzburgite (10%), wehrlite (5%), eclogite (10%), spinel lherzolite (30%), garnet/spinel lherzolite (10%), and garnet lherzolite (15%). Olivine, orthopyroxene, clinopyroxene, spinel, and garnet compositions were determined using the electron microprobe. A variety of geothermometers and geobarometers were used (see [12] for details) to calculate the pressure and temperature of equilibration for the various mantle

xenoliths. The calculated pressure versus the Mg# values of the xenolith olivines for the garnet/spinel lherzolite, fertile garnet lherzolite, and depleted garned lherzolite are plotted in Figure 31. The fertile versus depleted lherzolites are distinguished on the basis of the garnet chemistry and textural relationships. Garnets from the depleted lherzolites have high Cr content (3 to 8% Cr_2O_3) and kelyphite rims. The high Cr content indicates a previous melting event while the kelyphite rims formed during retrograde metamorphism (the enrichment event). The olivines in the depleted garnet lherzolite have greater mg#s than those in the fertile garnet lherzolite. The mg#s for olivines from the Prairie Creek lamproite fall between those of the fertile and depleted garnet lherzolite. The depleted garnet lherzolite field extends to pressures required for diamond formation. The lamproite magmas were probably generated at a pressure of ~6 GPa (a depth of 150 to 180 km) and temperatures in excess of 1200 °C, based on maximum recorded xenolith pressures and extrapolation of the ~40 mW/m^2 mantle geotherm [12].

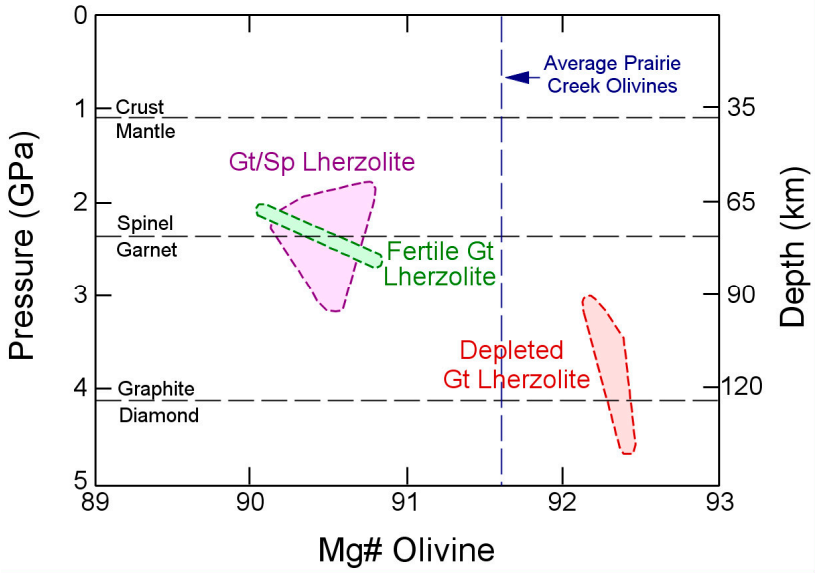

Figure 31. Pressure (GPa) plotted versus mg# of olivines from lherzolite xenoliths. The other mantle xenoliths are not plotted on this diagram as they come from shallower depths. The average mg# for the Prairie Creek olivines falls between those of the fertile and depleted garnet lherzolite. An olivine crystallizing from a melt in equilibrium with the depleted olivine garnet lherzolite would have a similar olivine mg#.

The trace element and isotopic data support the inference that the lamprophyre melts were derived from an enriched mantle source (HIMU/EMII). The HIMU source is related to recycled oceanic crust while the EMII source is related to sediment-enriched recycled crustal materials [99]. Boron isotope data obtained for carbonatite and silicate samples from the Magnet Cove complex indicated that the source region contained recycled crustal material [100].

Trace element concentrations can be used to model melt sources and degree of melting. Both the lamproite and lamprophyre melts are derived from garnet-bearing lherzolite. However, the characteristics of the sources and the melting regime are different. These differences are assessed using REEs. The computer program IGPET [101] is used for the modeling exercise. For the lamproites representative REE data are from the depleted subcontintental lithosphere of the Siberian craton [102] and for the lamprophyres the representative REE data are from calculated values for the various OIB reservoirs [90]. Mantle mineralogy for the subcontinental lithosphere is from [12] while a global average is used for the OIB source. Mineral proportions entering the melt are from [103] using the 3 GPa melting equation for the lamprophyres and the 7 GPa equation for the lamproites. REE par-

tition coefficients for garnet lherzolite minerals are from [104]. The results of the modeling are shown in Figure 32. Both models do a reasonable job of reproducing the shape of the REE patterns (2% partial melt for the lamproites and 7% partial melt for the lamprophyres) but absolute abundances are about 50% of the measured abundances. This implies that the actual sources have significantly greater REE abundances than the reference sources.

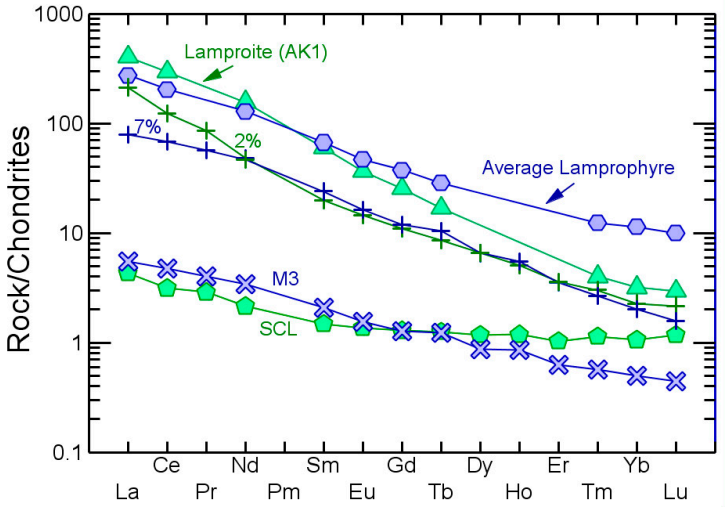

Figure 32. REE models for melting of lamproite and lamprophyre garnet lherzolite sources. The shape of the REE patterns, but not the absolute abundances, can be modeled by 2% melting of a depleted garnet lherzolite (lamproites) and by 7% melting of an OIB-like source (lamprophyres). REE abundances for SCL from [102] and OIB source (M3 reservoir) from [90]. Chondrite normalization values from [71].

6.2. Phonolites, Trachytes, and Syenites

6.2.1. Major Element Chemistry and Phase Equilibria

Although broadly similar chemically (Figure 23), the coarse-grained and fine-grained felsic rocks differ in detail. On the TAS classification diagram (Figure 22) the fine-grained felsic rocks plot in the phonolite and trachyte fields. Almost all are silica-undersaturated. On the plutonic classification diagram the coarse-grained felsic rocks are classified as foidolites and various types of foid rocks. All are silica-undersaturated. For both the volcanic and plutonic rocks the major element chemistry is similar (Figure 23). However, the phase relations are different for the plutonic vs. volcanic rocks and there are systematic trace element differences, particularly in the case of Ba and Sr (Figure 26c,d) between the various felsic rock suites.

On the nepheline–albite–orthoclase–kalsilite phase diagram [105,106] (Figure 33a) the felsic dike rocks and the Granite Mountain and Saline County syenites fall along cotectics: alkali feldspar–leucite and alkali feldspar–nepheline. The phonolites plot near the 1 Kbar ternary minimum while a number of the Granite Mountain–Saline County–Benton felsic dikes plot near the 1 bar ternary minimum. The phase relations support the inference that the bulk rock compositions of these samples approximate liquid compositions. Apatite saturation temperatures [107] for the Granite Mountain syenites and most of the felsic dikes range from 700 to 900 °C. One of the phonolites and the three Saline County syenite samples have Tapsat ranging from 550 to 600 °C. Apatite saturation temperatures generally decline as SiO_2 declines (Figure 33b), consistent with the approach to the Ne–Or–Ab minimum at low pressure. The Magnet Cove felsic rocks lie along a trend extending from the leucite first to the nepheline first field (Figure 33c). Only a few samples plot along the leucite–nepheline cotectic and none plot near the ternary minimum in this system. The pseudoleucite syenites fall in the leucite first field (but note that the size of these fields is pressure-dependent) as

do a number of the other syenites. For the garnet-nepheline syenite the distribution is best described as a linear trend extending from the leucite field to nepheline (the gray nepheline field shown on the diagram is based on the analyses reported in this paper) and can be interpreted as a mixture of liquid and nepheline. Some of the Diamond Joe nepheline syenites also fall along this trend. For the garnet-nepheline syenites and the nepheline syenites there is a rough negative correlation between apatite saturation temperatures and SiO_2 (Figure 33d). Biotite calculated temperatures, although fewer in number, tend to agree with the apatite saturation temperatures. The notable exceptions are the samples with apatite saturation temperatures less than 650 °C.

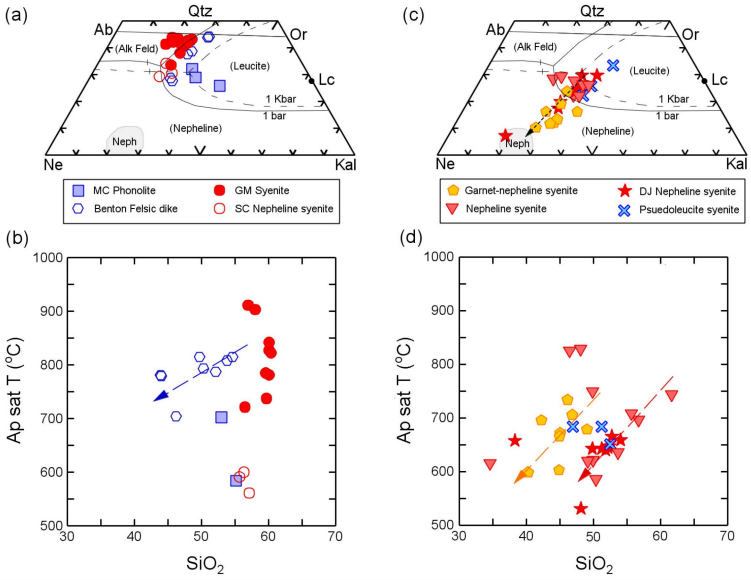

Figure 33. Nepheline–albite–orthoclase–quartz [105,106] phase diagram showing the locations of the 1 bar and 1 Kbar cotectics and invariant points and apatite saturation temperatures versus SiO_2. (**a**) Plot of felsic dikes and Granite Mountain–Saline County syenites. The samples plot on or near the various cotectics and invariant points (note the effect of pressure) which suggests that these samples approximate liquid compositions. The gray field encompasses the nepheline chemistries determined in this study. (**b**) Apatite saturation temperatures [107] versus SiO_2 for the felsic dikes and Granite Mountain–Saline County syenites. There is a general pattern of decreasing temperature with decreasing SiO_2 as expected for liquids that are evolving towards the silica-undersaturated minimum in this system. (**c**) Plot of various nepheline syenites from Magnet Cove which define an apparent mixing line between a ternary liquid and nepheline. (**d**) Apatite saturation temperatures [107] versus SiO_2 for the Magnet Cove nepheline syenites.

6.2.2. Trace Elements

Because the compositions of these rocks falls outside the calibration for the widely used thermodynamic models, these models cannot be used to investigate the evolution of the syenitic magmas. Instead, trace element modeling is used to assess the role of fractional crystallization/crystal accumulation in the evolution of the magmas. Isotopic data indicates that there was no significant crustal involvement (Figure 30) in the evolution of these magmas and AFC and similar processes will not be considered. Based on the petrography the most likely fractionating/accumulating phases are alkali feldspar, plagioclase, nepheline, pyroxene, and garnet. Micas and amphiboles are probably not early crystallizing phases. Titanite and the various oxide minerals can play a role in the evolution of certain elemental concentrations but are present in small amounts and will not be considered here.

Trace element models consider the variation between the Eu anomaly (Eu/Eu*) and Ba, Sr, and the La/Yb ratio. Ba and Sr concentrations are largely controlled by the fractional crystallization of the feldspar minerals. The La/Yb ratio is largely controlled by the

fractionation of clinopyroxene and garnet. For the modeling exercise—alkali feldspar (Or = 75), plagioclase (An = 35), clinopyroxene (Di = 20), QFM = 0, and T = 900 °C. In order to calculate the changes in the Eu anomaly as a function of fractional crystallization Eu^{2+} and Eu^{3+} values must be known for the melt. An average phonolite composition was used for this calculation and the approach of [108] was used to determine the Eu^{2+}/Eu^{3+} ratio. Optical basicity was determined using the Duffy–Ingram approach [109,110]. Partition coefficients were calculated using the Onuma parabola and the elastic properties of a mineral [111,112]. Partition coefficients for some of the mineral phases and elements were taken from the literature: plagioclase/phonolite for Sr [113], nepheline/phonolite [114], and garnet/phonolite [59]. The graphical results are found in Figure 34.

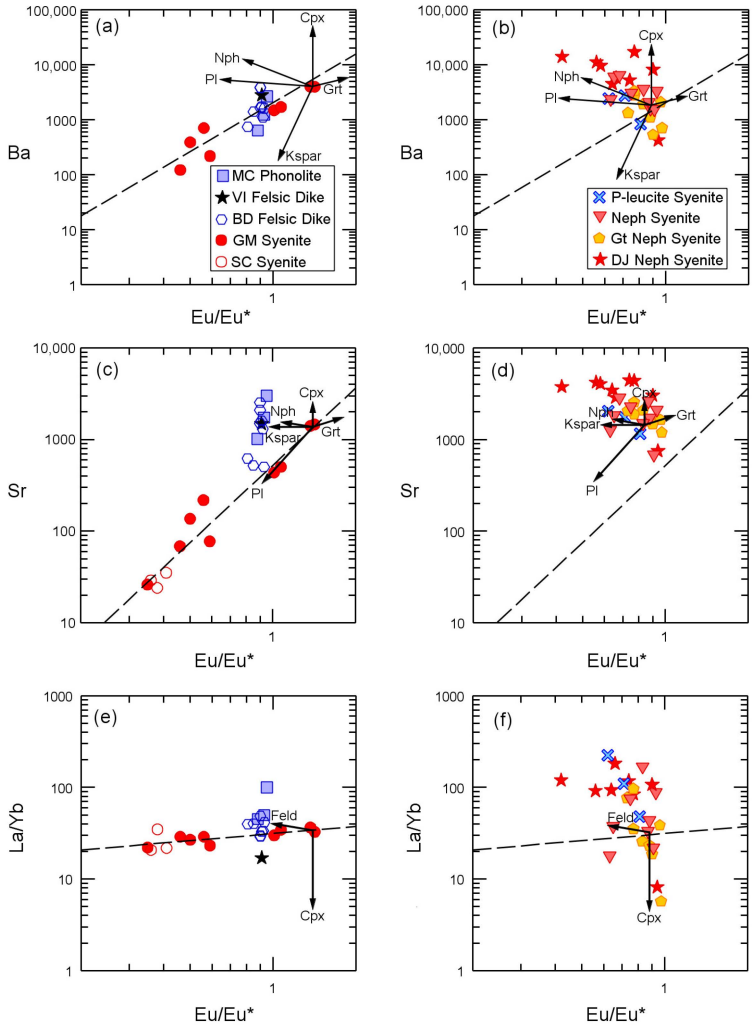

Figure 34. Plots of log Eu/Eu* versus log various elemental concentrations and elemental ratios. On these types of plots, rocks that are related by fractional crystallization will fall along straight lines. Arrows show fractionation trends controlled by different minerals. The dashed line on each diagram is the trend defined by the Granite Mountain–Saline County syenites. (**a**) Barium—felsic dikes and Granite Mountain and Saline County syenites. (**b**) Barium—Magnet Cove syenites. (**c**) Strontium—felsic dikes and Granite Mountain and Saline County syenites. (**d**) Strontium—Magnet Cove syenites. (**e**) La/Yb ratio—felsic dikes and Granite Mountain and Saline County syenites. (**f**) La/Yb ratio—Magnet Cove Syenites. Only two fractionation vectors are shown on the La/Yb plots because alkali feldspar, plagioclase, and nepheline have essentially the same fractionation trend. Pyroxene and garnet also have essentially the same fractionation trend.

The evolution of the felsic dikes is largely controlled by clinopyroxene fractionation (Figure 34a,c,e) as evidenced by the excellent correlation with the clinopyroxene

fractionation vectors. The coeval lamprophyre dikes invariably have clinopyroxene phenocrysts which supports this inference. On the nepheline–quartz–kalsilite phase diagram (Figure 33a) the felsic dike rocks plot in the alkali feldspar or nepheline first fields and apparently lie along a cotectic located between 1 bar and 1 Kbar. Despite this thermodynamic-based prediction of alkali feldspar and/or nepheline crystallization, the chemical differentiation of these magmas appears to be largely controlled by clinopyroxene crystallization.

The Granite Mountain and Saline County syenites fall between the alkali feldspar and plagioclase fractionation trends, suggesting that these two minerals played a major role in the evolution of the magma (Figure 34a,c,e). The small decline in the La/Yb ratios with an increasingly negative Eu anomaly also suggests that clinopyroxene played a minor role in the evolution of the magma (Figure 34e). On the nepheline–quartz–kalsilite phase diagram (Figure 33a) the syenites plot along a low-temperature cotectic, some samples fall in the feldspar first field, and a cluster of samples are found near the ternary minimum. Note that the samples that plot near the ternary minimum are completely depleted in Ba and have little Sr, indicating that these samples represent extreme differentiation.

The Magnet Cove syenites have distinctly different trace element distributions (Figure 34b,d,f). On the nepheline–quartz–kalsilite phase diagram these samples plot in the leucite and nepheline fields (Figure 33c). Many samples lie along an apparent mixing line from the cluster in the leucite field to the composition of the nepheline in the rocks. In terms of the trace elements, because of the scatter in the data, trends are not clearly defined. The Diamond Joe samples fall between the nepheline and clinopyroxe vectors, in agreement with the mineralogy of these rocks (essentially nepheline and pyroxene). The garnet-nepheline syenite samples broadly plot between the nepheline and garnet fractionation vectors. The phase equilibria relationships suggest that these rocks do not represent liquid compositions but rather are mixtures of liquid and crystals. The trace element distributions will depend on the relative contributions of liquid and the various mineral phases so scatter in the elemental plots is expected.

The three Saline County syenites and one of the Granite Mountain syenites (GM6) are distinguished from the other samples on the basis of their plotting at the 1 bar ternary minimum (Figure 33a) and being essentially depleted in Ba and Sr (Figure 34a,c). Texturally, the samples are coarse-grained to pegmatitic. All the samples contain astrophyllite, instead of biotite, which indicates that the magmatic phase was peralkaline and Ti + Fe- and F-rich [53]. Two of the Saline County pegmatitic syenites show unusual V-shaped REE patterns (Figure 25e) which are sometimes referred to as the "tetrad effect" [115,116]. This effect is often ascribed to strong complexation in evolved systems that leads to formation of a F^--, Cl^--, CO_3^{2-}-, B-rich fluid [117–119]. Experimental studies also show that in alkali-rich melts late-stage residual magmas at low temperature can evolve a F-rich immiscible fluid [120]. Thus, the samples with the V-shaped REE patterns were produced by the late-stage crystallization of F- and alkali-rich melts.

6.2.3. Magma Sources

Mafic rocks are rare in the AAP and surface and near surface exposures are mostly lamprophyres. Pyroxenites are found in the subsurface in the Benton area. Geophysical data suggest that there may be a connection at depth between the Magnet Cove, Potash Sulphur Springs, and V-intrusive and gravity modeling indicates higher-density rocks at depth which could represent a solidified mafic magma or accumulation of dense phases [7]. The carbonatites (ε_{Nd} = 4.2 ± 0.2 Magnet Cove, 3.7 Potash Sulphur Springs) and ijolites (ε_{Nd} = 4.0 ± 0.1 Magnet Cove) are isotopically similar [8]. There are no isotopic data for the felsic rocks at Magnet Cove. As discussed previously, the various syenites at Magnet Cove fractionated an assemblage of nepheline-clinopyroxene-(±) garnet (Figure 34b). The ijolites

at Magnet Cove have the same mineral assemblage and may represent the fractionates formed during the evolution of the syenites. If this is the case, the syenites would have the same isotopic signature as the ijolites. For the lamprophyres $\varepsilon_{Nd} = 3.6 \pm 0.1$ [8]. The Granite Mountain Syenites have $\varepsilon_{Nd} = 2.4 \pm 0.1$ and the Saline County syenite has $\varepsilon_{Nd} = 1.8$ [8]. The various rock types are isotopically similar, but the lower ε_{Nd} values for the syenites may indicate some crustal contamination. As previously discussed, the lamprophyres have trace element and isotopic signatures typical of an OIB source.

With the exception of the Benton dike swarm, the paucity of exposed mafic rocks makes it difficult to determine the composition of the original melt that formed the felsic rocks. Lamprophyres, felsic (phonolite) dikes, and pyroxenites occur at Benton. The pyroxenites were only encountered in drill core. It is possible that these rocks are related, i.e., the pyroxenites represent cumulates from a lamprophyric magma.

Felsic and lamprophyre dike chemistry (new data reported in this study) and average values for mica pyroxenite and pyroxenite are plotted on chondrite- and primitive-mantle-normalized diagrams (Figure 35). Compared to the lamprophyre dikes, the felsic dikes are much more enriched in silica (lamprophyre SiO_2 avg = 41.61, felsic dike SiO_2 avg = 49.32) and total alkalis (lamprophyre $Na_2O + K_2O$ avg = 4.44, felsic dike $Na_2O + K_2O$ avg = 9.71). Despite these significant differences in major element abundances, the chondrite-normalized plots are very similar (Figure 35a). The primitive-mantle-normalized plot (Figure 35b) shows several notable differences—the lamprophyres are much more enriched in Cs and Ba. Fractionation of a mineral assemblage similar to that of the pyroxenites can explain many of the differences in the lamprophyre vs. felsic dike chemistry, e.g., decrease in P and increase in HREEs in the felsic dikes relative to the lamprophyres. However, this simple model cannot explain the significant decreases in Cs and Ba in the felsic dikes relative to the lamprophyres.

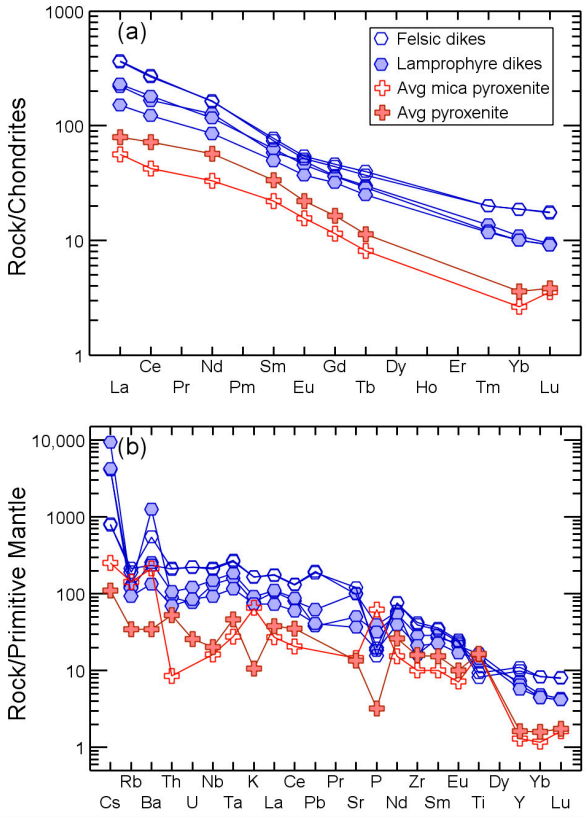

Figure 35. Normalized plots for Benton felsic and lamprophyre dikes, average mica pyroxenite, and average pyroxenite. (**a**) Chondrite-normalized REE plot. (**b**) Primitive-mantle-normalized plot. Chondrite normalization values from [71] and Primitive Mantle normalization values from [72].

6.3. Carbonatites

Carbonatites are found in four intrusions in the AAP—Magnet Cove, Potash Sulphur Springs, Perryville–Morrilton, and the Benton dike swarm. The Potash Sulphur Springs carbonatite is essentially calciocarbonatite while the Magnet Cove and Benton carbonatites are calciocarbonatites trending to magnesiocarbonatites (Figure 19). The Perryville–Morrilton occurrence consists of xenocrystic alvikite breccia that contains xenoliths of granite, syenite, magnetite-apatite rock, sovite, phlogopitite, and argillite [35]. The carbonatites are minor components of these various intrusions, are intruded late in the crystallization sequence, and frequently intermingle with pre-existing silicate rocks.

The origin of carbonatites is an ongoing discussion in the petrologic literature [121–124]. There are three main models: (1) residual melts of fractionated nephelinite or melilitite magmas, (2) silicate–carbonate melt immiscibility, and (3) primary magmas produced by the melting of carbonated peridotite. Hybrid versions of these models are also used [121]. For example, models (1) and (2) can be combined. Consider a residual nephelinite or melilitite magma that has evolved to an alkali and CO_2-rich residue which enters a field of silicate–carbonate immiscibility.

Initial Sr, Nd, Hf, and Pb isotopic ratios have been determined for AAP carbonatites and associated silicate rocks [8,44,92]. To maintain internal consistency the isotopic comparisons use the data in [8] and the comparisons are limited to the Sr and Nd isotopic systems (Table 1). In terms of Nd isotopes, the carbonatite and ijolite at Magnet Cove (MC) are isotopically identical and could be part of the same system. The carbonatite at Potash Sulphur Springs (PSS) and the lamprophyres from the V-intrusive (VI) and Benton dike swarm (BD) have essentially identical values. The Magnet Cove carbonatites and ijolites and Potash Sulphur Springs carbonatite have similar Sr isotopic values. The lamprophyres from the V-intrusive and Benton dike swarm have similar Sr isotopic values that are distinctly different from those of the Magnet Cove and Potash Sulphur Springs samples. In the following discussion it is assumed that the Magnet Cove and Potash Sulphur Springs carbonatites and silicate rocks are part of the same isotopic system and the V-intrusive and Benton dike swarm silicate rocks belong to a different isotopic system. Thus for Magnet Cove (and perhaps Potash Sulphur Springs) the isotopic data are permissible for silicate–carbonatite liquid immiscibility. Unfortunately the isotopic composition of the Benton carbonatites is unknown.

Table 1. Comparison of Sr and Nd isotopic data for AAP carbonatites and associated silicate rocks [1].

Lithology and Location	$^{87}Sr/^{86}Sr_i$	εSr	εNd
Carbonatite (MC)	0.703770 ± 0.000265	-9.9 ± 3.7	4.2 ± 0.1
Ijolite (MC)	0.703695 ± 0.000193	-10.9 ± 2.8	4.0 ± 0.1
Carbonatite (PSS)	0.703788	−9.6	3.7
Lamprophyre (VI)	0.704606	2.0	3.5
Lamprophyre (BD)	0.704791	4.7	3.7

[1] Data from [8].

In Section 5.2.1 a variety of elemental relationships were investigated. Of particular note (Figure 21c) is the inverse relationship between CaO and SiO_2. Coupled with the apparent mixing lines between carbonatite and diopside/phlogopite (Figure 21b) and the petrographic observation that the carbonatite melt invades and partially disaggregates pre-existing silicate rock, it is suggested that most of the carbonatite samples represent a mixture of silicate minerals and carbonatite liquid. For each carbonatite locality, the two samples with highest CaO content (and lowest SiO_2), and therefore presumably closest to the pure carbonatite liquid, are selected for further interpretation.

Figure 36 shows chondrite-normalized REE (Figure 36a) and primitive-mantle-normalized (Figure 36b) plots. For comparison, also shown are the average values for Oldoinyo Lengai [125], the only active carbonatitic volcano, and the calculated primary carbonatite magma for the Fort Portal extrusive carbonatite [73]. Oldoinyo Lengai has a much larger La/Yb ratio (more enriched in the LREEs) than Fort Portal or the AAP carbonatites. The Benton carbonatite patterns, as is one of the Potash Sulphur Springs patterns, are similar to Fort Portal, but with a relative enrichment in the HREEs. The other three samples have lower total REEs and tend to be convex downwards. Apatite is abundant in the carbonatites, and fractionation of apatite will relatively deplete the middle REEs, leading to convex downward REE patterns [126,127]. On the spider diagram the Fort Portal pattern, with some exceptions (Magnet Cove carbonatite), is similar to that of the AAP carbonatites. Notable anomalies in the patterns are relative depletion in Th, K, P, Zr, and Ti and relative enrichment in Ba and Sr. The Oldoinyo Lengai carbonatite is significantly enriched in both Sr and Ba compared to the other carbonatites which are less enriched in Ba. The other notable, and exhaustively discussed, difference is the high concentration of alkalis in the Oldoinyo Lengai magmas (which are classified as natrocarbonatite [125]) compared to other carbonatites.

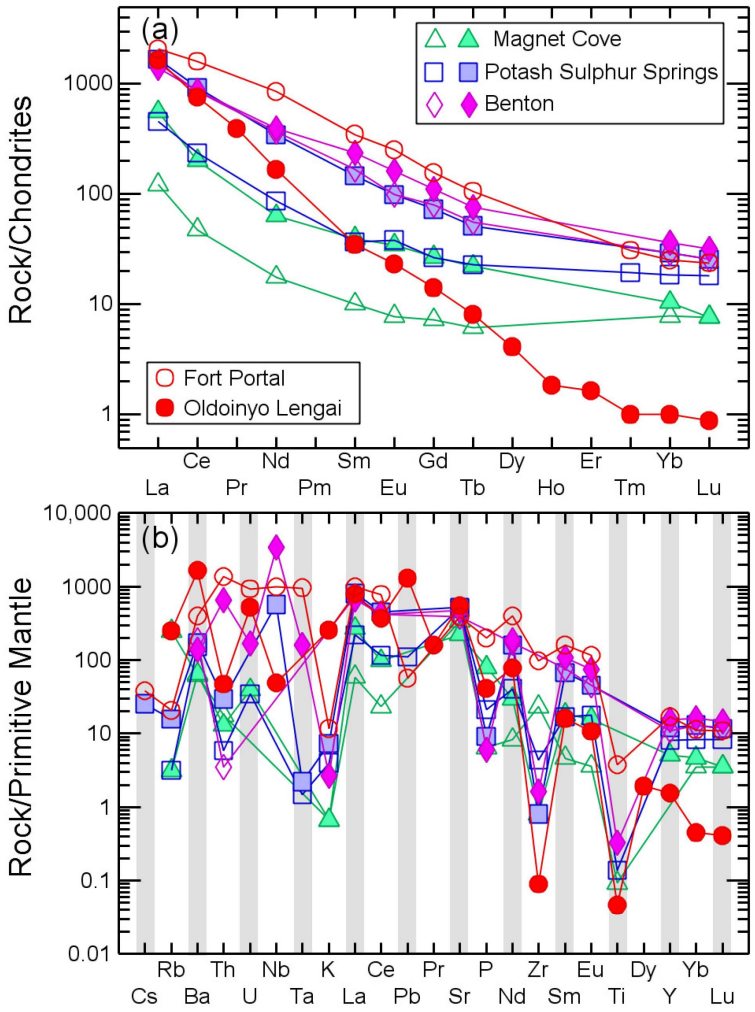

Figure 36. Normalized plots Oldoinyo Lengai [125], Fort Portal [73], and selected AAP carbonatites. (**a**) Chondrite-normalized REE plot. (**b**) Primitive-mantle-normalized plot. Chondrite normalization values from [71] and Primitive Mantle normalization values from [72].

Liquid immiscibility which occurs at some point during the crystallization and evolution of a CO_2-rich mantle-derived magma is a frequently used model to explain the

origin of carbonatites [122,124]. For the AAP the phonolites and lamprophyres that occur with the carbonatites are the most likely silicate half of an immiscible silicate–carbonate pair. The compositions of the silicate rocks and the most evolved carbonatite samples are projected into the $SiO_2 + TiO_2 + Al_2O_3 - Na_2O + K_2O - CaO + FeO + MgO$ phase diagram [122,128–131] (Figure 37). For comparison, also shown on the diagram are the compositions of melt inclusions representing immiscible liquid pairs from Oldoinyo Lengai and Kerimasi and solvus curves for various pressures and temperatures. The AAP carbonatites plot in the alkali-poor, Ca-Fe-Mg-rich corner of the phase diagram as do the majority of magmatic carbonatites [132]. The calculated immiscible carbonate liquid for the Fort Portal extrusive carbonatite plots in the same location. The silicate liquid half of the Fort Portal immiscible pair plots near the Benton lamprophyres. Based on these observations it is concluded that the AAP carbonatites may have originated by the separation of a CO_2-rich liquid from a lamprophyric melt.

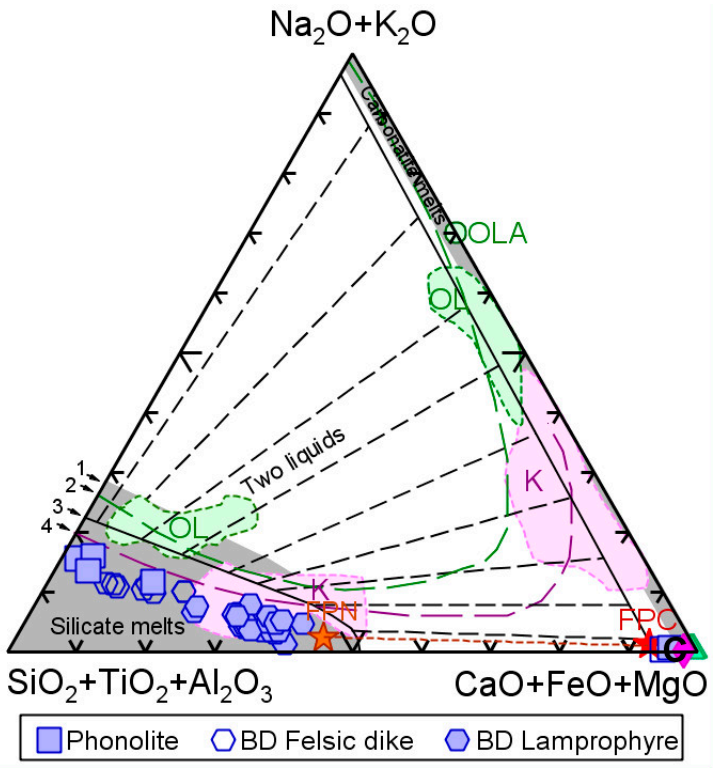

Figure 37. Phonolite, felsic dikes, lamprophyre dikes, and selected carbonatite compositions projected into the $SiO_2 + TiO_2 + Al_2O_3 - Na_2O + K_2O - CaO + FeO + MgO$ diagram [131]. C—selected AAP carbonatites which cluster in the CaO + FeO + MgO corner of the diagram. Solvus curves from [130,133,134]. 1—500 MPa, 1250 °C solvus [128], 2—100 MPa, 700 °C solvus [134], 3—boundary at 500 MPa, 1250 °C based on natural pairs [128], 4—500 MPa, 900–1000 °C solvus [133]. FPC—calculated Fort Portal carbonatite liquid and FPN—coexisting Fort Portal nephelinite magma [73], K—fields for silicate and carbonatite melt inclusions for Kerimasi [129], OL—fields for silicate and carbonatite melt inclusions from Oldoinyo Lengai and OLA average composition of Oldoinyo Lengai carbonatite [135–137].

Further intepretation of the origin of the AAP carbonatites is not possible given the limited amount of data for the carbonate phase. Surface exposures of carbonatite are sparse with most of the samples coming from drill cores. The variety of alkaline rock types and the two distinct carbonatite trends—calciocarbonatite and magnesiocarbonatite—suggest that a detailed study of the AAP carbonatites, if the drill cores are available, is warranted.

6.4. Synthesis of Magmatic History

Three distinct periods of magmatism are recorded in the Arkansas alkaline province. The first occurs at ~104 Ma and is characterized by the intrusion of lamproite magmas, the second occurs at ~100 Ma and is characterized by the intrusion of a variety of alkaline mafic rocks (lamprophyres, ijolites, pyroxenites), nepheline syenites and phonolites, and carbonatites, and the third occurs at ~88 Ma and is characterized by the intrusion of a relatively large nepheline syenite–syenite body not accompanied by the intrusion of mafic igneous rocks. The lamproite magmas are derived from a subcontinental depleted lithospheric mantle and based on xenolith data the magmas originated at a depth of greater than 120 km (Figure 31, [12]). The magmas for the two younger periods of igneous activity were extracted from a mixed HIMU-EM asthenospheric source (Figure 30).

A Middle Cretaceous erosion surface separates basement rocks from the overlying Upper Cretaceous–Holocene sediments of the Mississippi embayment [138]. This erosion surface indicates that there was a regional uplift that was time synchronous with the emplacement of the various AAP intrusions. A lithospheric cross-section, developed on the basis of gravity, seismic, drill core, and geologic data [139], passes just west of the AAP (Figure 38). The notable features of this transect include the upward deflection of the MOHO under the AAP and the presence of a mafic intrusion (density $\approx$ 3050 kg m^{-3}) extending from 15 to 30 km. Diorite, gabbro, ijolite, meltegite, and alkali basalt fall in this density range [140]. Alkali basalt is the most likely lithology and may represent the mafic precursor that gave rise to the more differentiated rocks of the AAP. Gravity and magnetic data were used to develop a two- and three-dimensional model of the Magnet Cove complex [21]. The complex extends to a depth of 20 km, widens out at midcrustal depths, and may be connected to other intrusions in the AAP. A key observation is the alignment of the Magnet Cove intrusion with pre-existing structures that may be controlled by the Precambrian crystalline basement and the ocean–continent transition zone (Figure 38, "Transitional Crust") beneath the AAP. A geomagnetic survey of the bauxite region in central Arkansas (the deposits associated with the Granite Mountain and Saline County syenites) indicated a subsurface areal extent of 1036 km^2 and the presence of subsurface magnetic highs which may represent more mafic igneous intrusions [141]. With the exception of the Prairie Creek lamproites, mafic igneous rocks (mostly lamprophyres) are sparsely exposed both at the surface and in drill core. The geophysical data, however, suggest that mafic igneous rocks may exist at depth below the AAP.

A number of petrogenetic models have been proposed for the origin of the AAP: (1) passage of the continental plate over a hotspot [4–6], (2) activation of zones of lithospheric weakness due to far field stress [7,21], (3) sheet-like mantle upwellings induced along slab window margins [8], and (4) edge-driven convection [9,92]. Any successful model must explain the three discrete periods of magmatism, each with its own distinctive suite of rocks—(1) lamproites, (2) carbonatites, lamprophyres, phonolites, syenites, and ijolites, and (3) nepheline syenites without associated mafic igneous rocks. The igneous activity starts with the emplacement of lamproites (1) derived from a subcontinental lithospheric source at a depth of more than 120 km. Approximately four million years later association (2) magmas are emplaced and geochemical and isotopic data indicate derivation from an OIB-like source. We suggest that the rise of asthenospheric mantle (the source of the ~100 Ma magmas) from greater depth provided the heat energy for the melting of the subcontinental lithosphere. Assuming that the lamproite magma was generated at a depth of 140 km and that the present day apex of the upper mantle is at 25 km, the rising asthenospheric mantle must transit a vertical distance of 115 km in 4 million years. This gives a rise rate of ~2.9 cm y^{-1} which is in the range of rates determined for convecting asthenospheric mantle [142]. The association (3) magmas were emplaced 10 million years

later. Isotopic and trace element data support the contention that these melts were also derived from a similar OIB-like source and were not significantly contaminated during their rise into the crust. The nepheline syenites of association (3) were probably derived by differentiation of a more mafic magma. Arguments against the hotspot model were previously presented [7] and will not be discussed here. Models involving upwelling along slab window margins and edge-driven convection are broadly similar in that they involve magmatism associated with subducting slabs. In a general way these two models fit the observed relationships, but the time-progressive change in the depth of melting and the time hiatus between associations (2) and (3) is not well explained by these models. The AAP is a relatively small igneous province that is confined to a tectonically active zone that went through multiple cycles of collision and extension [21]. The province is localized in a boundary zone between the Precambrian craton and the Ouachita Mountain fold belt and underlain by transitional crust (Figure 38). The temporal sequence—deep lithosphere-sourced lamproites followed ~4 Myr later by OIB-like mafic–felsic association, then a ~10 Myr pause before large nepheline syenite intrusions without coeval mafic rocks—fits reactivation of a pre-existing lithospheric weakness under far-field stress [7,21,143], with transient asthenospheric upwelling supplying heat/melt. Hotspot track and slab window variants explain parts of the record but do not naturally produce the observed hiatus and depth-of-melting progression.

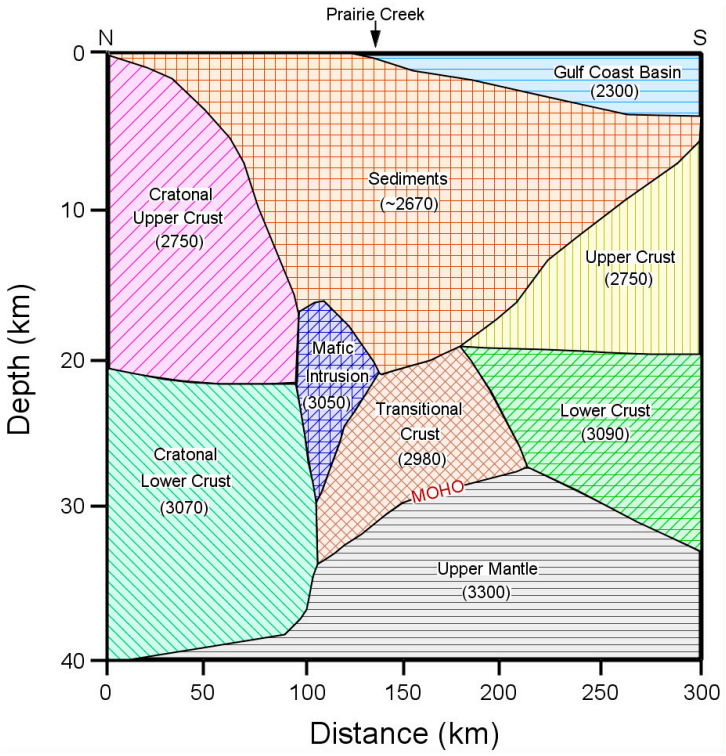

Figure 38. Lithospheric cross-section located slightly west of the Prairie Creek lamproite. Numbers in parentheses are rock densities in kg m^{-3}. The Moho is convex upwards, indicating the rise of asthenospheric mantle. Cross-section modified from [13].

Supplementary Materials: The following supporting information can be downloaded at: https://www.mdpi.com/article/10.3390/min15111133/s1, Table S1: Compilation of radiometric ages [144,145]; Table S2: Mineral data compilation; Table S3: Compilation of element and isotopic data.

Author Contributions: Conceptualization, N.E.; methodology, N.E. and N.C.; software, N.E. and N.C.; validation, N.E., N.C., G.T., and L.B.; formal analysis, N.E., N.C., G.T., and L.B.; investigation, N.E., N.C., G.T., and L.B.; resources, N.E. and N.C.; data curation, N.E.; writing—original draft preparation,

N.E.; writing—review and editing, N.E., N.C., G.T., and L.B.; visualization, N.E.; supervision, N.E.; project administration, N.E. All authors have read and agreed to the published version of the manuscript.

Funding: This research received no external funding.

Data Availability Statement: The data used for this study are found in the Supplemental Data Tables S2 and S3.

Acknowledgments: The XRF major element data were obtained at the University of Queensland with the assistance of F. Aubrey. S. Eby determined the LOI values for the samples. The XRF trace element data were obtained at the University of Oxford with the assistance of K. Parrish. The Instrumental neutron activation analyses (INAAs) were performed at the University of Massachusetts Lowell Radiation Laboratory. The invaluable support of the Radiation Laboratory staff is greatly appreciated.

Conflicts of Interest: The authors declare no conflicts of interest.

References

1. Byerly, G.R. Igneous Activity. In *The Gulf of Mexico Basin, The Geology of North America*; Salvador, A., Ed.; Geological Society of America: Boulder, CO, USA, 1991; Volume J, pp. 91–108.
2. Kidwell, A.L. Mesozoic Igneous Activity in the Northern Gulf Coastal Plain. *Trans. Gulf Coast Assoc. Geol. Soc.* **1951**, *1*, 182–199.
3. Baksi, A.K. The Timing of Late Cretaceous Alkalic Igneous Activity in the Northern Gulf of Mexico Basin, Southeastern USA 1. *J. Geol.* **1997**, *105*, 629–643. [CrossRef]
4. Morgan, W.J. Hotspot Tracks and the Early Rifting of the Atlantic. *Tectonophysics* **1983**, *94*, 123–139. [CrossRef]
5. Duncan, R.A. Age Progressive Volcanism in the New England Seamounts and the Opening of the Central Atlantic Ocean. *J. Geophys. Res. Solid Earth* **1984**, *89*, 9980–9990. [CrossRef]
6. Muller, R.D.; Royer, J.-Y.; De Geodynamique, L.; Mer, V.S.; Lawrence, F.; Lawver, A. Revised Plate Motions Relative to the Hotspots from Combined Atlantic and Indian Ocean Hotspot Tracks. *Geology* **1993**, *21*, 275–278. [CrossRef]
7. Eby, G.N.; Vasconcelos, P. Geochronology of the Arkansas Alkaline Province, Southeastern United States. *J. Geol.* **2009**, *117*, 615–626. [CrossRef]
8. Duke, G.I.; Carlson, R.W.; Frost, C.D.; Hearn, B.C.; Eby, G.N. Continent-Scale Linearity of Kimberlite-Carbonatite Magmatism, Mid-Continent North America. *Earth Planet. Sci. Lett.* **2014**, *403*, 1–14. [CrossRef]
9. Kjarsgaard, B.A.; Heaman, L.M.; Sarkar, C.; Pearson, D.G. The North America Mid-Cretaceous Kimberlite Corridor: Wet, Edge-Driven Decompression Melting of an OIB-Type Deep Mantle Source. *Geochem. Geophys. Geosystems* **2017**, *18*, 2727–2747. [CrossRef]
10. Arbenz, J.K. The Ouachita System. In *The Geology of North America*; Bally, A.W., Palmer, A.R., Eds.; Geological Society of America: Boulder, CO, USA, 1989; Volume A, pp. 371–396.
11. Waldman, M.; McCandless, T.; Dummett, H. Geology and Petrography of the Twin Knobs #1 Lamproite, Pike County, Arkansas. In *Mantle Metasomatism and Alkaline Magmatism*; Morris, E., Pasteris, J., Eds.; Geological Society of America: Boulder, CO, USA, 1987; Volume 215, pp. 205–216.
12. Dunn, D.P. Xenolith Mineralogy and Geology of the Prairie Creek Lamproite Province, Arkansas. Ph.D. Thesis, University of Texas at Austin, Austin, TX, USA, 2002.
13. Dunn, D.P. Arkansas Crustal Xenoliths: Implications for Basement Rocks of the Northern Gulf Coast, USA. *Lithosphere* **2009**, *1*, 60–64. [CrossRef]
14. Howard, J.M.; Hanson, W.D. *Geology of the Crater of Diamonds State Park and Vicinity, Pike County, Arkansas*; State Park Series 03; Arkansas Geological Survey: North Little Rock, AR, USA, 2008; pp. 1–14.
15. Hendrix, B.L. Crater of Diamonds: Jewel of Arkansas. In *Crater of Diamonds: Jewel of Arkansas*; Arkansas Geological Survey: North Little Rock, AR, USA, 1989; pp. 1–40.
16. Lewis, R.D.; Meyer, H.O.A.; Bolivar, S.L.; Brookins, D.G. Mineralogy of the Diamond-Bearing "Kimberlite", Murfreesboro, Arkansas. In Proceedings of the EOS 57; American Geophysical Union: Washington, DC, USA, 1976; p. 761.
17. Whitney, D.L.; Evans, B.W. Abbreviations for Names of Rock-Forming Minerals. *Am. Mineral.* **2010**, *95*, 185–187. [CrossRef]
18. Erickson, R.L.; Blade, L.V. *Geochemistry and Petrology of the Alkalic Igneous Complex at Magnet Cove, Arkansas*; Professional Paper; United States Government Printing Office: Washington, DC, USA, 1963.
19. Flohr, M.J.K.; Ross, M. Alkaline Igneous Rocks of Magnet Cove, Arkansas: Mineralogy and Geochemistry of Syenites. *Lithos* **1990**, *26*, 67–98. [CrossRef]

20. Howard, M. Guidebook to the Central Arkansas Alkalic Province—The View after Nearly 150 Years of Investigation. In *2000 South-Central GSA Guidebook*; Geological Society of America: Boulder, CO, USA, 2000; pp. 1–27.
21. Amaral, C.M.; Lamb, A.P.; Dumond, G. Geophysical Characterization of an Alkaline-carbonatite Complex Using Gravity and Magnetic Methods at Magnet Cove, Arkansas, USA. *Tectonophysics* **2024**, *893*, 230545. [CrossRef]
22. Flohr, M.; Ross, M. Alkaline Igneous Rocks of Magnet Cove, Arkansas: Metasomatized Ijolite Xenoliths from Diamond Jo Quarry. *Am. Mineral.* **1989**, *74*, 113–131.
23. Howard, M. Transition Element Geochemistry and Petrography of the Potash Sulphur Springs Intrusive Complex, Garland County, Arkansas. Master's Thesis, University of Arkansas, Fayetteville, AR, USA, 1974.
24. Heathcote, R. Fenitization of the Arkansas Novaculite and Adjacent Intrusive, Garland County, Arkansas. Master's Thesis, University of Arkansas, Fayetteville, AR, USA, 1974.
25. Heathcote, R.C.; McCormick, G.R. Major-Cation Substitution in Phlogopite and Evolution of Carbonatite in the Potash Sulphur Springs Complex, Garland County, Arkansas. *Am. Mineral.* **1989**, *74*, 132–140.
26. Flohr, M.; Howard, J.M. *Geochemical Data of Alkaline Igneous Rocks and Carbonatites, Potash Sulphur Springs Igneous Complex, Arkansas*; United States Geological Survey: Reston, VA, USA,, 1995; OFR 95-836; pp. 1–13.
27. Owens, D. Bedrock Geology of the "V" Intrusive, Garland County, Arkansas. Master's Thesis, University of Arkansas, Fayetteville, AR, USA, 1968.
28. Robison, E. Geochemistry of Lamprophyric Rocks of the Eastern Ouachita Mountains, Arkansas. Master's Thesis, University of Arkansas, Fayetteville, AR, USA, 1976.
29. Valdovinos, D. Petrography of Some Lamprophyres of the Eastern Ouachita Mountains of Arkansas. Master's Thesis, University of Arkansas, Fayetteville, AR, USA, 1968.
30. Flohr, M.J.; Howard, J.M. *Geochemical Data of Drill Core Samples of Carbonatites and Associated Igneous Rocks, Benton, Arkansas*; United States Geological Survey: Reston, VA, USA, 1994; OFR 94-450; pp. 1–21.
31. Gordon, M.; Tracey, J.I.; Ellis, M.W. *Geology of the Arkansas Bauxite Region*; United States Geological Survey Professional Paper 299; United States Geological Survey: Reston, VA, USA, 1958; pp. 1–268.
32. Bath, T. *Igneous Lamination and Layering in the Nepheline Syenite Quarry, Sec/36, T1S, R14W Saline County, Arkansas*; University of Arkansas: Fayetteville, AR, USA, 1980.
33. Morris, E. The Cretaceous Arkansas Alkalic Province: A Summary of Petrology and Geochemistry. In *Geological Society of America Special Paper 215*; Morris, E.M., Pasteris, J.D., Eds.; Geological Society of America: Boulder, CO, USA, 1987; pp. 217–233. ISBN 9780813722153.
34. Barwood, H.L. Mineralogy of the Granite Mountain Syenite. *Rocks Miner.* **1989**, *64*, 314–322. [CrossRef]
35. McCormick, G.R.; Heathcote, R.C. Mineral Chemistry and Petrogenesis of Carbonatite Intrusions, Perry and Conway Counties, Arkansas. *Am. Mineral.* **1987**, *72*, 59–66.
36. Zartman, R.E.; Brock, M.R.; Heyl, A.V.; Thomas, H.H. K-Ar and Rb-Sr Ages of Some Alkalic Intrusive Rocks from Central and Eastern United States. *Am. J. Sci.* **1967**, *265*, 848–870. [CrossRef]
37. Gogineni, S.V.; Melton, C.E.; Giardini, A.A. Some Petrological Aspects of the Prairie Creek Diamond-Bearing Kimberlite Diatreme, Arkansas. *Contrib. Mineral. Petrol.* **1978**, *66*, 251–261. [CrossRef]
38. Baldwin, O.D.; Adams, J.A.S. K40/Ar40 Ages of the Alkalic Igneous Rocks of the Balcones Fault Trend of Texas. *Tex. J. Sci.* **1971**, *22*, 223–231.
39. Arne, D. Evidence from Apatite Fission-Track Analysis for Regional Cretaceous Cooling in the Ouachita Mountain Fold Belt and Arkoma Basin of Arkansas: Geologic Note (1). *Am. Assoc. Pet. Geol. Bull.* **1992**, *76*, 392–402. [CrossRef]
40. Pell, D. In-Situ U-Pb Geochronology of Perovskite and Schorlomite Garnet from Magnet Cove, AR: New Age Constraints on Alkaline Magmatism and Suitability as Reference Materials. Honors Thesis, University of Kansas, Lawrence, MA, USA, 2023.
41. Scharon, L.; Hsu, I.C. Paleomagnetic Investigation of Some Arkansas Alkalic Igneous Rocks. *J. Geophys. Res.* **1969**, *74*, 2774–2779. [CrossRef]
42. Zartman, R.; Howard, J.M. Uranium-Lead Age of Large Zircon Crystals from the Potash Sulfur Springs Igneous Complex, Garland County, Arkansas. In *Mantle Metasomatism and Alkaline Magmatism*; Morris, E.M., Pasteris, J.D., Eds.; Geological Society of America: Boulder, CO, USA, 1987; Volume 215, pp. 235–240. ISBN 9780813722153.
43. Sarkar, S.; Dalton, H.; Giuliani, A.; Phillips, D.; Graham Pearson, D.; Nowell, G.M.; Woodhead, J.D.; Hergt, J.; Maas, R.; Lynton Jaques, A.; et al. Extreme Enriched-Mantle (EM) Compositions Recorded by the Sr-Nd-Hf Isotopes of Global Cratonic Lamproites. *Geochim. Cosmochim. Acta* **2025**, *394*, 220–243. [CrossRef]
44. Tilton, G.R.; Kwon, S.T.; Frost, D.M. Isotopic Relationships in Arkansas Alkalic Complexes. In *Mantle Metasomatism and Alkaline Magmatism*; Morris, E.M., Pasteris, J.D., Eds.; Geological Society of America: Boulder, CO, USA, 1987; Volume 215, pp. 241–248.
45. Flohr, M.J.K. Titanium, Vanadium, and Niobium Mineralization and Alkali Metasomatism from the Magnet Cove Complex, Arkansas. *Econ. Geol.* **1994**, *89*, 105–130. [CrossRef]

46. Lambert, D.D.; Shirey, S.B.; Bergman, S.C. Proterozoic Lithospheric Mantle Source for the Prairie Creek Lamproites: Re-Os and Sm-Nd Isotopic Evidence. *Geology* **1995**, *23*, 273–276. [CrossRef]
47. Flohr, M.; Howard, J.M. *Geochemical Data of Drill Core Samples of Carbonatites and Associated Igneous Rocks, Magnet Cove Complex, Arkansas*; United States Geological Survey: Reston, VA, USA, 1995; OFR 95-621; pp. 1–14.
48. Wilson, A.D. A New Method for the Determination of Ferrous Iron in Rocks and Minerals. *Bull. Geol. Surv. Great Br.* **1955**, *9*, 56–58.
49. Walters, J.B.; Gies, N.B. MinPlotX: A Powerful Tool for Formula Recalculation, Visualization, and Comparison of Large Mineral Compositional Datasets. *Mineralogia* **2025**, *56*, 13–22. [CrossRef]
50. Hawthorne, F.C.; Oberti, R.; Harlow, G.E.; Maresch, W.V.; Martin, R.F.; Schumacher, J.C.; Welch, M.D. Ima Report: Nomenclature of the Amphibole Supergroup. *Am. Mineral.* **2012**, *97*, 2031–2048. [CrossRef]
51. Li, X.; Zhang, C. Machine Learning Thermobarometry for Biotite-Bearing Magmas. *J. Geophys. Res. Solid Earth* **2022**, *127*, e2022JB024137. [CrossRef]
52. Tindle, A.G.; Webb, P.C. Estimation of Lithium Contents in Trioctahedral Micas Using Microprobe Data: Application to Micas from Granitic Rocks. *Eur. J. Miner.* **1990**, *2*, 595–610. [CrossRef]
53. Piilonen, P.C.; Lalonde, A.E.; Mcdonald, A.M.; Gault, R.A.; Larsen, A.O. Insights into Astrophyllite-Group Minerals. 1. Nomenclature, Composition and Development of a Standardized General Formula. *Can. Mineral.* **2003**, *41*, 1–26. [CrossRef]
54. Nekvasil, H. Ternary Feldspar Crystallization in High-Temperature Felsic Magmas. *Am. Mineral.* **1992**, *77*, 592–604.
55. Hamilton, D. Nephelines as Crystallization Temperature Indicators. *J. Geol.* **1961**, *69*, 321–329. [CrossRef]
56. Henderson, D.M.B. Nepheline solid solution compositions: Stoichiometry revisited, reviewed, clarified and rationalised. *Mineral. Mag.* **2020**, *84*, 813–838. [CrossRef]
57. Chen, W.; Zhang, W.; Simonetti, A.; Jian, S. Mineral Chemistry of Melanite from Calcitic Ijolite, the Oka Carbonatite Complex, Canada: Implications for Multi-Pulse Magma Mixing. *J. Earth Sci.* **2016**, *27*, 599–610. [CrossRef]
58. Dawson, J.B. Peralkaline Nephelinite-Natrocarbonatite Relationships at Oldoinyo Lengai, Tanzania. *J. Petrol.* **1998**, *39*, 2077–2094. [CrossRef]
59. Melluso, L.; Scarpati, C.; Zanetti, A.; Sparice, D.; de' Gennaro, R. The Petrogenesis of Chemically Zoned, Phonolitic, Plinian and Sub-Plinian Eruptions of Somma-Vesuvius, Italy: Role of Accessory Phase Removal, Independently Filled Magma Reservoirs with Time, and Transition from Slightly to Highly Silica Undersaturated Magmatic Series in an Ultrapotassic Stratovolcano. *Lithos* **2022**, *430–431*, 106854. [CrossRef]
60. Kowallis, B.J.; Christiansen, E.H.; Dorais, M.J.; Winkel, A.; Henze, P.; Franzen, L.; Mosher, H. Variation of Fe, Al, and F Substitution in Titanite (Sphene). *Geosciences* **2022**, *12*, 229. [CrossRef]
61. Webster, J.D.; Tappen, C.M.; Mandeville, C.W. Partitioning Behavior of Chlorine and Fluorine in the System Apatite-Melt-Fluid. II: Felsic Silicate Systems at 200 MPa. *Geochim. Cosmochim. Acta* **2009**, *73*, 559–581. [CrossRef]
62. Piccoli, P.; Candela, P. Apatite in Igneous Systems. In *Phosphates—Geochemical, Geobiological, and Materials Importance*; Kohn, M., Rakovan, J., Hughes, J., Eds.; Mineralogical Society of America: Chantilly, VA, USA, 2002; pp. 255–292.
63. Andersen, D.; Lindsley, D. Internally Consistent Solution Models for Fe-Mg-Mn-Ti Oxides: Fe-Ti Oxides. *Am. Mineral.* **1988**, *73*, 714–726.
64. Mitchell, R.H. *Kimberlites*; Springer: Boston, MA, USA, 1986; ISBN 978-1-4899-0570-3.
65. Mitchell, R.H. *Kimberlites, Orangeites, and Related Rocks*; Springer: Boston, MA, USA, 1995; ISBN 978-1-4613-5822-0.
66. Roeder, P.L.; Schulze, D.J. Crystallization of Groundmass Spinel in Kimberlite. *J. Petrol.* **2008**, *49*, 1473–1495. [CrossRef]
67. Wones, D.R.; Gilbert, M.C. The Fayalite-Magnetite-Quartz Assemblage between 600 and 800 C. *Am. J. Sci.* **1969**, *267-a*, 480–488. [CrossRef]
68. Carmichael, I.S.E.; Nicholls, J. Iron-Titanium Oxides and Oxygen Fugacities in Volcanic Rocks. *J. Geophys. Res.* **1967**, *72*, 4665–4687. [CrossRef]
69. Eugster, H.P.; Wones, D.R. Stability Relations of the Ferruginous Biotite, Annite. *J. Petrol.* **1962**, *3*, 82–125. [CrossRef]
70. Woolley, A.R.; Kempe, D.R.C. Carbonatites: Nomenclature, Average Chemical Composition. In *Carbonatites: Genesis and Evolution*; Bell, K., Ed.; Unwin Hyman: London, UK, 1989; pp. 1–14.
71. Nakamura, N. Determination of REE, Ba, Fe, Mg, Na and K in Carbonaceous and Ordinary Chondrites. *Geochim. Cosmochim. Acta* **1974**, *38*, 757–775. [CrossRef]
72. Sun, S.-s.; McDonough, W.F. Chemical and Isotopic Systematics of Oceanic Basalts: Implications for Mantle Composition and Processes. In *Magmatism in the Ocean Basins*; Saunders, A.D., Norry, M.J., Eds.; Geological Society of London: London, UK, 1989; Volume 42, pp. 313–345.
73. Eby, G.N.; Lloyd, F.E.; Woolley, A.R. Geochemistry and Petrogenesis of the Fort Portal, Uganda, Extrusive Carbonatite. *Lithos* **2009**, *113*, 785–800. [CrossRef]

74. Le Maitre, R.; Bateman, P.; Dudek, A.; Keller, J.; Lameyre, J.; Le Bas, M.; Sabine, P.; Schmid, R.; Sorensen, H.; Streckeisen, A.; et al. *A Classification of Ingeous Rocks and Glossary of Terms: Recommendations of the International Union of Geological Sciences Subcommission on the Systematics of Ingeous Rocks*; Le Maitre, R., Ed.; Blackwell: Oxford, UK, 1989.
75. Middlemost, E.A.K. Naming Materials in the Magma/Igneous Rock System. *Earth Sci. Rev.* **1994**, *37*, 215–224. [CrossRef]
76. Olin, P.H.; Wolff, J.A. Partitioning of Rare Earth and High Field Strength Elements between Titanite and Phonolitic Liquid. *Lithos* **2012**, *128–131*, 46–54. [CrossRef]
77. Rudnick, R.L.; Gao, S. Rudnick_Gao_Treatise. *Treatise Geochem.* **2003**, *3*, 1–64.
78. Sack, R.O.; Walker, D.; Carmichael, I.S.E. Experimental Petrology of Alkalic Lavas: Constraints on Cotectics of Multiple Saturation in Natural Basaltic Liquids. *Contrib. Mineral. Petrol.* **1987**, *96*, 1–23. [CrossRef]
79. Boudreau, A.E. PELE—A Version of the MELTS Software Program for the PC Platform. *Comput. Geosci.* **1999**, *25*, 201–203. [CrossRef]
80. Suikkanen, E. EasyMelts 0.2.x Beta 2020. Available online: https://magmasource.caltech.edu/gitlist/easyMelts.git (accessed on 9 August 2021).
81. LaTourrette, T.; Hervig, R.L.; Holloway, J.R. Trace Element Partitioning between Amphibole, Phlogopite, and Basanite Melt. *Earth Planet. Sci. Lett.* **1995**, *135*, 13–30. [CrossRef]
82. Roeder, P.L.; Emslie, R.F. Olivine-Liquid Equilibrium. *Contrib. Mineral. Petrol.* **1970**, *29*, 275–289. [CrossRef]
83. Grove, T.L.; Bryan, W.B. Fractionation of Pyroxene-Phyric MORB at Low Pressure: An Experimental Study. *Contrib. Mineral. Petrol.* **1983**, *84*, 293–309. [CrossRef]
84. Sisson, T.W.; Grove, T.L. Temperatures and H2O Contents of Low-MgO High-Alumina Basalts. *Contrib. Mineral. Petrol.* **1993**, *113*, 167–184. [CrossRef]
85. Krmíček, L.; Chalapathi Rao, N.V. Lamprophyres, Lamproites and Related Rocks as Tracers to Supercontinent Cycles and Metallogenesis. In *Geological Society Special Publication*; Geological Society of London: London, UK, 2022; Volume 513, pp. 1–16.
86. Krmícek, L.; Cempírek, J.; Havlín, A.; Prichystal, A.; Houzar, S.; Krmícková, M.; Gadas, P. Mineralogy and Petrogenesis of a Ba-Ti-Zr-Rich Peralkaline Dyke from Šebkovice (Czech Republic): Recognition of the Most Lamproitic Variscan Intrusion. *Lithos* **2011**, *121*, 74–86. [CrossRef]
87. Pearce, J.A. Geochemical Fingerprinting of Oceanic Basalts with Applications to Ophiolite Classification and the Search for Archean Oceanic Crust. *Lithos* **2008**, *100*, 14–48. [CrossRef]
88. Downes, H. Formation and Modification of the Shallow Sub-Continental Lithospheric Mantle: A Review of Geochemical Evidence from Ultramafic Xenolith Suites and Tectonically Emplaced Ultramafic Massifs of Western and Central Europe. *J. Petrol.* **2001**, *42*, 233–250. [CrossRef]
89. Akbari, M.; Ghorbani, M.R.; Cousens, B.L.; Graham, I.T. A Robust Discrimination Scheme for Ocean Island Basalts Based on Ce/Rb, Tb/La, and Ba/Nb Ratios. *Chem. Geol.* **2023**, *628*, 121486. [CrossRef]
90. Naumov, V.B.; Girnis, A.V.; Dorofeeva, V.A. Melts of Ocean Island Basalts (OIB) and Their Sources: Evidence from Melt Inclusions and Quenched Glasses of Rocks. *Petrology* **2025**, *33*, 94–111. [CrossRef]
91. Rollinson, H.; Pease, V. *Using Geochemical Data*; Cambridge University Press: Cambridge, UK, 2021; ISBN 9781108777834.
92. Walker, S.R.; Çemen, I.; Wielicki, M.W.; Tew, B.H.; Stockli, D. Edge-Driven Convection-Based Models for Evolution of the Mississippi Embayment and Associated Alkaline Magmatism. In *Extensional Tectonics: Rifting and Continental Extension: Volume 2: Tectonic Processes: A Global View*; Wiley: New York, NY, USA, 2025; Volume 2, pp. 199–228. ISBN 9781119773757.
93. Eby, N. Monteregian Hills I. Petrography, Major and Trace Element Geochemistry, and Strontium Isotopic Chemistry of The Western Intrusions: Mounts Royal, St. Bruno, and Johnson. *J. Petrol.* **1984**, *25*, 421–452. [CrossRef]
94. Roulleau, E.; Stevenson, R. Geochemical and Isotopic (Nd-Sr-Hf-Pb) Evidence for a Lithospheric Mantle Source in the Formation of the Alkaline Monteregian Province (Quebec). *Can. J. Earth Sci.* **2013**, *50*, 650–666. [CrossRef]
95. Zindler, A.; Hart, S. Chemical Geodynamics. *Ann. Rev. Earth Planet. Sci.* **1986**, *14*, 493–571. [CrossRef]
96. Stracke, A. Earth's Heterogeneous Mantle: A Product of Convection-Driven Interaction between Crust and Mantle. *Chem. Geol.* **2012**, *330–331*, 274–299. [CrossRef]
97. Chauvel, C.; Lewin, E.; Carpentier, M.; Arndt, N.T.; Marini, J.C. Role of Recycled Oceanic Basalt and Sediment in Generating the Hf-Nd Mantle Array. *Nat. Geosci.* **2008**, *1*, 64–67. [CrossRef]
98. Jones, R.E.; van Keken, P.E.; Hauri, E.H.; Tucker, J.M.; Vervoort, J.; Ballentine, C.J. Origins of the Terrestrial Hf-Nd Mantle Array: Evidence from a Combined Geodynamical-Geochemical Approach. *Earth Planet. Sci. Lett.* **2019**, *518*, 26–39. [CrossRef]
99. Willbold, M.; Stracke, A. Trace Element Composition of Mantle End-Members: Implications for Recycling of Oceanic and Upper and Lower Continental Crust. *Geochem. Geophys. Geosystems* **2006**, *7*, 1–30. [CrossRef]
100. Ozkaya, O. Geochemical, Isotopic and Chronological Investigation of the Magnet Cove Carbonatite Complex, Arkansas, USA. Master's Thesis, University of Notre Dame, Notre Dame, IN, USA, 2020.
101. Carr, M.J.; Gazel, E. Igpet Software for Modeling Igneous Processes: Examples of Application Using the Open Educational Version. *Miner. Pet.* **2017**, *111*, 283–289. [CrossRef]

102. Ionov, D.A.; Doucet, L.S.; Ashchepkov, I.V. Composition of the Lithospheric Mantle in the Siberian Craton: New Constraints from Fresh Peridotites in the Udachnaya-East Kimberlite. *J. Petrol.* **2010**, *51*, 2177–2210. [CrossRef]
103. Walter, M.J. Melting of Garnet Peridotite and the Origin of Komatiite and Depleted Lithosphere. *J. Petrol.* **1998**, *39*, 29–60. [CrossRef]
104. Feigenson, M.D.; Patino, L.C.; Carr, M.J. Constraints on Partial Melting Imposed by Rare Earth Element Variations in Mauna Kea Basalts. *J. Geophys. Res. Solid Earth* **1996**, *101*, 11815–11829. [CrossRef]
105. Henderson, C.M.B. Feldspathoid Stabilities and Phase Inversions-A Review. In *Feldspars and Feldspathoids, Structures, Properties and Occurrences*; Brown, W.L., Ed.; D. Reidel Publishing Company: Dordrecht, The Netherlands, 1984; pp. 471–499.
106. Gittins, J. The Feldspathoidal Alkaline Rocks. In *The Evolution of the Igneous Rocks*; Yoder, H., Ed.; Princeton University Press: Princeton, NJ, USA, 1979; pp. 351–390.
107. Harrison, T.M.; Watson, E.B. The Behavior of Apatite during Crustal Anatexis: Equilibrium and Kinetic Considerations. *Geochim. Cosmochim. Acta* **1984**, *48*, 1467–1477. [CrossRef]
108. Burnham, A.D.; Berry, A.J.; Halse, H.R.; Schofield, P.F.; Cibin, G.; Mosselmans, J.F.W. The Oxidation State of Europium in Silicate Melts as a Function of Oxygen Fugacity, Composition and Temperature. *Chem. Geol.* **2015**, *411*, 248–259. [CrossRef]
109. Duffy, J.; Ingram, M. Comments on the Application of Optical Basicity to Glass. *J. Non Cryst. Solids* **1992**, *144*, 76–80. [CrossRef]
110. Duffy, J.A. A Review of Optical Basicity and Its Applications to Oxidic Systems. *Geochlmica Cosmochim. Acta* **1993**, *51*, 3961–3970. [CrossRef]
111. Blundy, J.; Wood, B. Prediction of Crystal–Melt Partition Coefficients from Elastic Moduli. *Nature* **1994**, *372*, 452–454. [CrossRef]
112. Onuma, N.; Higuchi, H.; Wakita, H.; Nagasawa, H. Trace Element Partition between Two Pyroxenes and the Host Lava. *Earth Planet. Sci. Lett.* **1968**, *5*, 47–51. [CrossRef]
113. Nielsen, R.L.; Ustunisik, G.; Weinsteiger, A.B.; Tepley, F.J.; Johnston, A.D.; Kent, A.J.R. Trace Element Partitioning between Plagioclase and Melt: An Investigation of the Impact of Experimental and Analytical Procedures. *Geochem. Geophys. Geosystems* **2017**, *18*, 3359–3384. [CrossRef]
114. Dawson, J.B.; Hinton, R.W.; Steele, I.M. The Composition of Anorthoclase and Nepheline in Mount Kenya Phonolite and Kilimanjaro Trachyte, and Crystal-Glass Partitioning of Elements. *Can Miner.* **2008**, *46*, 1455–1464. [CrossRef]
115. Nugent, L.J. Theory of the Tetrad Effect in the Lanthanide(III) and Actinide(III) Series. *J. Inorg. Nucl. Chem.* **1970**, *32*, 3485–3491. [CrossRef]
116. McLennan, S.M. Rare Earth Element Geochemistry and the "Tetrad" Effect. *Geochim. Cosmochim. Acta* **1994**, *58*, 2025–2033. [CrossRef]
117. Irber, W. The Lanthanide Tetrad Effect and Its Correlation with K/Rb, Eu/Eu∗, Sr/Eu, Y/Ho, and Zr/Hf of Evolving Peraluminous Granite Suites. *Geochim. Cosmochim. Acta* **1999**, *63*, 489–508. [CrossRef]
118. Veksler, I.V.; Dorfman, A.M.; Kamenetsky, M.; Dulski, P.; Dingwell, D.B. Partitioning of Lanthanides and Y between Immiscible Silicate and Fluoride Melts, Fluorite and Cryolite and the Origin of the Lanthanide Tetrad Effect in Igneous Rocks. *Geochim. Cosmochim. Acta* **2005**, *69*, 2847–2860. [CrossRef]
119. Bau, M. Controls on the Fractionation of Isovalent Trace Elements in Magmatic and Aqueous Systems: Evidence from Y/Ho, Zr/Hf, and Lanthanide Tetrad Effect. *Contrib. Mineral. Petrol.* **1996**, *123*, 323–333. [CrossRef]
120. DolejS, D.; Baker, D.R. Liquidus Equilibria in the System K2O-Na2O-Al2O3-SiO2-F2O-1-H2O to 100 MPa: I. Silicate-Fluoride Liquid Immiscibility in Anhydrous Systems. *J. Petrol.* **2007**, *48*, 785–806. [CrossRef]
121. Jones, A.P.; Genge, M.; Carmody, L. Carbonate Melts and Carbonatites. *Rev. Miner. Geochem.* **2013**, *75*, 289–322. [CrossRef]
122. Schmidt, M.W.; Giuliani, A.; Poli, S. The Origin of Carbonatites—Combining the Rock Record with Available Experimental Constraints. *J. Petrol.* **2024**, *65*, egae105. [CrossRef]
123. Weidendorfer, D.; Schmidt, M.W.; Mattsson, H.B. A Common Origin of Carbonatite Magmas. *Geology* **2017**, *45*, 507–510. [CrossRef]
124. Yaxley, G.M.; Anenburg, M.; Tappe, S.; Decree, S.; Guzmics, T. Carbonatites: Classification, Sources, Evolution, and Emplacement. *Annu. Rev. Earth Planet. Sci.* **2025**, *50*, 261–293. [CrossRef]
125. Keller, J.; Zaitsev, A.N. Geochemistry and Petrogenetic Significance of Natrocarbonatites at Oldoinyo Lengai, Tanzania: Composition of Lavas from 1988 to 2007. *Lithos* **2012**, *148*, 45–53. [CrossRef]
126. Guo, H.; Tuduri, J.; Nabyl, Z.; Erdmann, S.; Li, X.; Gaillard, F. Rare Earth Elements in Apatite: A Proxy for Unravelling Carbonatite Melt Compositions. *Earth Planet. Sci. Lett.* **2024**, *642*, 118863. [CrossRef]
127. Klemme, S.; Dalpé, C. Trace-Element Partitioning between Apatite and Carbonatite Melt. *Am. Mineral.* **2003**, *88*, 639–646. [CrossRef]
128. Kjarsgaard, B.A.; Hamilton, D.L. Liquid Immiscibility and the Origin of Alkali-Poor Carbonatites. *Mineral. Mag.* **1988**, *52*, 43–55. [CrossRef]
129. Guzmics, T.; Mitchell, R.H.; Szabó, C.; Berkesi, M.; Milke, R.; Ratter, K. Liquid Immiscibility between Silicate, Carbonate and Sulfide Melts in Melt Inclusions Hosted in Co-Precipitated Minerals from Kerimasi Volcano (Tanzania): Evolution of Carbonated Nephelinitic Magma. *Contrib. Mineral. Petrol.* **2012**, *164*, 101–122. [CrossRef]

130. Brooker, R.A.; Kjarsgaard, B.A. Silicate-Carbonate Liquid Immiscibility and Phase Relations in the System SiO2-Na2O-Al2O3-Cao-Co2 at 0·1-2·5 GPa with Applications to Carbonatite Genesis. *J. Petrol.* **2011**, *52*, 1281–1305. [CrossRef]
131. Hamilton, D.L.; Freestone, I.C.; Dawson, J.B.; Donaldson, C.H. Origin of Carbonatites by Liquid Immiscibility. *Nature* **1979**, *279*, 52–54. [CrossRef]
132. Berndt, J.; Klemme, S. Origin of Carbonatites—Liquid Immiscibility Caught in the Act. *Nat. Commun.* **2022**, *13*, 2892. [CrossRef]
133. Kjarsgaard, B.A. Phase Relations of a Carbonated High-CaO Nephelinite at 0·2 and 0·5 GPa. *J. Petrol.* **1998**, *39*, 2061–2075. [CrossRef]
134. Kjarsgaard, B.A.; Hamilton, D.L.; Peterson, T.D. Peralkaline Nephelinite/Carbonatite Liquid Immiscibility: Comparison of Phase Compositions in Experiments and Natural Lavas from Oldoinyo Lengai. In *Carbonatite Volcanism*; Bell, K., Keller, J., Eds.; Springer: Berlin, Germany, 1995; Volume 4, pp. 163–190.
135. Sharygin, V.V.; Kamenetsky, V.S.; Zaitsev, A.N.; Kamenetsky, M.B. Silicate-Natrocarbonatite Liquid Immiscibility in 1917 Eruption Combeite-Wollastonite Nephelinite, Oldoinyo Lengai Volcano, Tanzania: Melt Inclusion Study. *Lithos* **2012**, *152*, 23–39. [CrossRef]
136. de Moor, J.M.; Fischer, T.P.; King, P.L.; Botcharnikov, R.E.; Hervig, R.L.; Hilton, D.R.; Barry, P.H.; Mangasini, F.; Ramirez, C. Volatile-Rich Silicate Melts from Oldoinyo Lengai Volcano (Tanzania): Implications for Carbonatite Genesis and Eruptive Behavior. *Earth Planet. Sci. Lett.* **2013**, *361*, 379–390. [CrossRef]
137. Mitchell, R.H.; Dawson, J.B. Carbonate-Silicate Immiscibility and Extremely Peralkaline Silicate Glasses from Nasira Cone and Recent Eruptions at Oldoinyo Lengai Volcano, Tanzania. *Lithos* **2012**, *152*, 40–46. [CrossRef]
138. Stearns, R. Cretaceous, Paleocene, and Lower Eocene Geologic History of Northern Mississippi Embayment. *Bull. Geol. Soc. Am.* **1957**, *66*, 1077–1100. [CrossRef]
139. Mickus, K.L.; Keller, G.R. Lithospheric Structure of the South-Central United States. *Geology* **1992**, *20*, 335. [CrossRef]
140. Carmichael, R.S. *Practical Handbook of Physical Properties of Rocks and Minerals*; Carmichael, R.S., Ed.; CRC Press: Boca Raton, FL, USA, 1989.
141. Stearn, N. A Geomagnetic Survey of the Bauxite Region in Central Arkansas. *Ark. Geol. Surv. Bull.* **1930**, *5*, 1–16.
142. Turcotte, D.; Schubert, G. *Geodynamics*, 3rd ed.; Cambridge University Press: Cambridge, UK, 2014; ISBN 9781107006539.
143. Vogt, P.R.; Foulger, G.R. Lithospheric Weakspots, Not Hotspots: New England-Quebec and Shenandoah Anorogenic Magmatism in the Context of Global Plate Tectonics, Intraplate Stress and LIPs. *Earth Sci. Rev.* **2025**, *260*, 104991. [CrossRef]
144. Zartman, R.E. Geochronology of Some Alkalic Rock Provinces in Eastern and Central United States. *Annu. Rev. Earth Planet Sci.* **1977**, *5*, 257–286. [CrossRef]
145. Steiger, R.H.; Jager, E. Subcommission on Geochronology: Convention on the use of Decay Constants in Geo- and Cosmochronology. *Earth Planet Sci.* **1977**, *36*, 359–362. [CrossRef]